JETP Letters, Vol. 76, No. 2, 2002, pp. 104–106. Translated from Pis'ma v Zhurnal Éksperimental'noĭ i Teoreticheskoĭ Fiziki, Vol. 76, No. 2, 2002, pp. 115–117.

Structural Model for Vitrification of Pure Metals

A. V. Evteev, A. T. Kosilov, and E. V. Levchenko

Voronezh State Technical University, Moskovskiĭ pr. 14, Voronezh, 394026 Russia

e-mail: mfm@ns1.vstu.ac.ru

Received June 11, 2002

Abstract—The model of iron with Pak–Doyama pair interatomic potential was used as an example to demonstrate by molecular dynamic calculations that the structural stabilization of an amorphous phase of pure metals is due to the formation of a percolation cluster composed of the interpenetrating and mutually contacting icosahedra whose vertices and centers are occupied by atoms. © *2002 MAIK "Nauka/Interperiodica".*

PACS numbers: 61.43.-j

The revelation of fundamental distinctions between the atomic structures of a melt and a metallic glass is one of the topical and as yet unsolved problems of vitrification physics. The reason is that the available diffraction methods of studying the structure of disordered materials give only a one-dimensional averaged pattern of atomic distribution in the form of structure functions, whereas the models suggested for the short-range order with random close packing of atoms (Bernal model) or coordination polyhedra (Frank–Casper model), though used successfully in the description of mutual arrangement of atoms in liquid and amorphous metals, leave the question of individual traits of structural organization open.

A considerable progress in modeling the structure of liquid and amorphous states of metallic systems and in developing the atomic mechanisms and their mutual transformations can be achieved by molecular dynamic (MD) computer simulation with the use of highly efficient and well-optimized algorithms and adequate interatomic potentials.

In this work, the results of MD calculation are presented for the structural transformations occurring upon heating model amorphous iron under isochoric conditions from the initial state of an "instantaneously frozen" melt.

The interatomic interaction was described using the empirical Pak–Doyama pair potential in the form of the fourth-degree polynomial [1]

$$\varphi(r) = -0.188917(r - 1.82709)^4 + 1.70192(r - 2.50849)^2 - 0.198294 \text{ eV} \quad (1)$$

(r is expressed in Å). The cutoff radius (distance at which the potential and its first derivative smoothly decrease to zero) is $r_c = 3.44$ Å. The parameters of this potential were determined from the data on elastic properties of α-Fe. The use of this potential for modeling liquid and amorphous iron provides good agreement between the calculated and experimental structural characteristics [2–4].

At first, the MD model was constructed for a liquid iron at $T = 1823$ K with a real density of 7030 kg/m^3 [5]. Random atomic close packing was taken as the initial structure. The model contained 100000 atoms in the main cube with the periodic boundary conditions. The initial atomic velocities corresponded to the Maxwell distribution. The method of MD calculation consisted in the numerical integration of the equations of motion with the time step $\Delta t = 1.523 \times 10^{-15}$ s following the Verlet algorithm [6]. The system was kept at the indicated temperature for 2000 time steps (isothermal conditions). Then the temperature restriction was removed, and the thermal equilibrium in the system was established during 4000 time steps at a constant internal energy (adiabatic conditions). The starting amorphous state was obtained by "instantaneous" quenching by the static relaxation (SR) of a model melt, whose density was preliminarily increased to 7800 kg/m^3 (because of the lack of experimental data, the density was chosen in accordance with the data for α-Fe [7] corrected by ~1% for amorphization).

The system was next isochorically heated at a rate of 4.4×10^{12} K/s. The cyclic heating procedure amounted to a stepped temperature increase by $\Delta T = 20$ K ($T_i = i\Delta T$), where T_i is the "ambient" temperature at the ith cycle), maintaining this temperature in the system for $1000 \times \Delta t$, and annealing for $2000 \times \Delta t$ under adiabatic conditions. Therefore, the duration of one cycle was $3000 \times \Delta t$ or 4.569×10^{-12} s. It should be noted that the temperature T of the system in the adiabatic conditions and the ambient temperature T_i did not coincide rigorously. After each cycle, the system was brought by the SR method to the state with $T = 0$ K, allowing the atoms to occupy equilibrium positions in the local potential wells. For the statically relaxed models, the potential energy (U_0) and the product of pressure by volume (P_0V) were calculated. This procedure made it possible

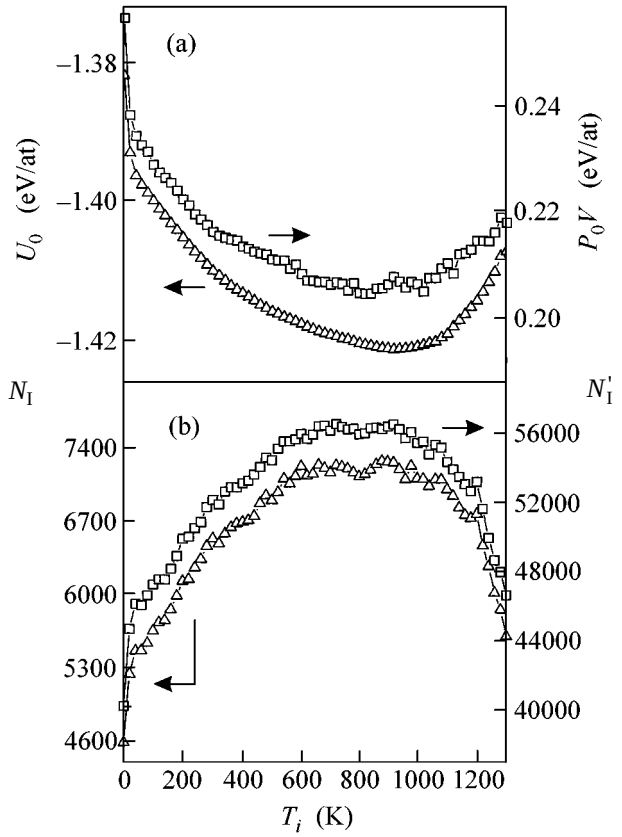

Fig. 1. Dependence on the ambient temperature T_i (a) for (△) the potential energy U_0 and (□) the product P_0V of pressure by volume in the iron model after static relaxation and (b) for (△) the number N_I of atoms located at the centers of icosahedra and (□) the overall number N_I' of atoms involved in the formation of icosahedra. Heating rate is 4.4×10^{12} K/s.

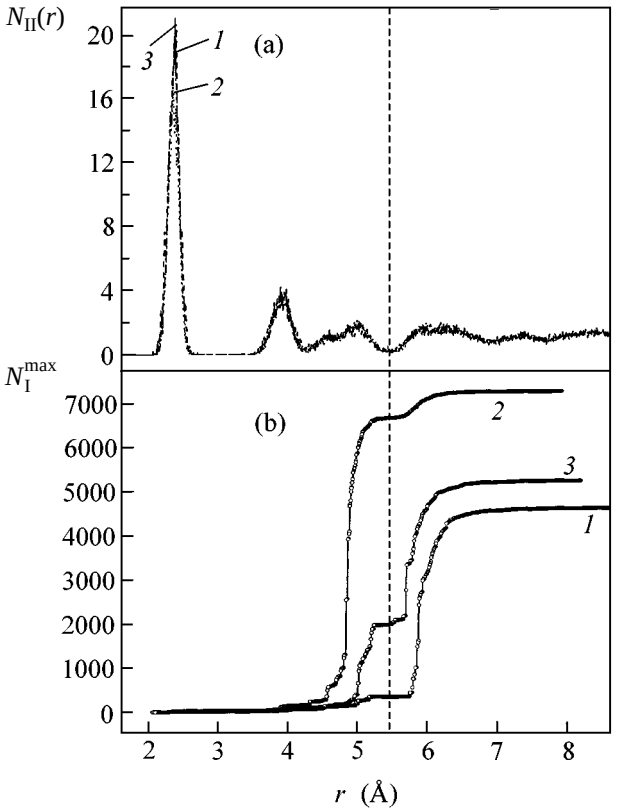

Fig. 2. (a) Pair radial distribution function $g_{II}(r)$ for the atoms located at the centers of icosahedra, and (b) the number N_I^{max} of such atoms in the largest cluster in which the distance between the neighbors is smaller than or equal to r. The dashed vertical line separates the regions corresponding (left) to the interpenetrating and contacting icosahedra and (right) to the isolated icosahedra. Curves *1*, *2*, and *3* correspond to ambient temperatures of 0, 920, and 1300 K, respectively.

to determine the degree of structural relaxation for the model with an increase in temperature.

One can see from Fig. 1a that the potential energy and the product of pressure by volume in the statically relaxed models decrease continuously during the course of the heating process as a result of an intense structural relaxation of the initial disordered phase. At $T \sim 920$ K, these dependences pass through a minimum and then increase monotonically with increasing temperature. At $T > 920$ K, the average overall atomic displacement increases drastically, indicating that the activation mechanism of atomic motion gives way to the activationless mechanism that is typical of the atomic diffusion in liquids [8].

To reveal the character of atomic rearrangement in the course of structural relaxation, the statistical and geometrical analyses were carried out on the basis of Voronoĭ polyhedra (VP). Since the icosahedron is energetically most stable among all coordination polyhedra in the close-packed structures and the presence of five-fold axes renders it incompatible with the translational symmetry, the formation of an amorphous structure in a pure metal with such coordination polyhedra hampers the atomic rearrangement in the crystallization process and, hence, provides a prerequisite for the stabilization of amorphous state. For this reason, we mainly focused on studying the evolution of structural elements with icosahedral symmetry during the process of isochronous annealing. Recall that each VP can be described by a set of numbers n_q that are equal to the number of faces with q sides (n_3-n_4-n_5-…) [9]. The VP for icosahedron is a pentagonal dodecahedron (0-0-12). It was established that, in the initial model of a frozen liquid, the fraction of atoms occupying the centers of icosahedra is 4.593%, and the total fraction of atoms involved in the formation of icosahedra is 40.276% (each icosahedron incorporates ~9 atoms on average) (Fig. 1b). In the structurally most completely relaxed model, these values amount at 920 K, respectively, to 7.258 and 56.502% (each icosahedron contains ~8 atoms on aver-

age), indicating that the number of atoms shared by several icosahedra increases.

Figure 2a shows the pair radial distribution functions $g_{II}(r)$ for the atoms located at the centers of icosahedra, as calculated for ambient temperatures of 0, 920, and 1300 K. It is worth noting that the form of this function is virtually independent of temperature. The first peak in $g_{II}(r)$ corresponds to the contact of interpenetrating icosahedra, the second peak corresponds to the sharing of their faces and edges, and the third (split) peak corresponds to the sharing of edges and vertices.

The use of percolation theory for studying the mutual arrangement of the atoms located at the centers of icosahedra (Fig. 2b) and the analysis or their pair radial distribution function (Fig. 2a) showed that the percolation cluster of mutually contacting icosahedra was absent in the frozen liquid, whereas it arose in the course of heating to 920 K and became denser due to the shift to smaller r values, and the number of icosahedra in the cluster increased. At a temperature of 920 K, the percolation cluster comprises both the interpenetrating icosahedra and the face-, edge-, and vertex-sharing icosahedra. Its fractal dimension is $D = 2.51$, and it incorporates 2536 icosahedra. However, an increase in the admissible distance between the neighboring atoms with icosahedral coordination leads to a rapid increase in the number of contacting icosahedra in the cluster and increase in its fractal dimension. In the range of distances corresponding to bond rupture between the icosahedra (dashed vertical line in Fig. 2), the fractal dimension is as high as $D = 2.992$, and the cluster comprises 6594 icosahedra formed by 49.649% of all atoms in the model. When recalculated to a volume of 1 mm^3, this value decreases to 45.613%. Heating above 920 K is accompanied by a decrease in the overall fraction of icosahedra (Fig. 1b) and by the ensuing decay of the percolation cluster of contacting icosahedra (Fig. 2b).

Thus, the percolation cluster composed of the translationally incompatible icosahedra involving almost a half of all atoms in the model plays the role of a binding framework that hampers the crystallization and, presumably, underlies the structural organization of a solid amorphous state of pure metals, which fundamentally distinguishes this state from a melt.

REFERENCES

1. H. M. Pak and M. Doyama, J. Fac. Eng., Univ. Tokyo, Ser. B **30**, 111 (1969).
2. R. Yamamoto, H. Matsuoka, and M. Doyama, Phys. Status Solidi A **45**, 305 (1978).
3. D. K. Belashchenko, Fiz. Met. Metalloved. **60**, 1076 (1985).
4. A. V. Evteev and A. T. Kosilov, Rasplavy, No. 1, 55 (1998).
5. A. A. Vertman and A. M. Samarin, *Properties of Iron Melts* (Nauka, Moscow, 1969).
6. L. Verlet, Phys. Rev. **159**, 98 (1967).
7. C. J. Smithells, *Metals Reference Book* (Butterworths, London, 1976; Metallurgiya, Moscow, 1980).
8. D. K. Belashchenko, Usp. Fiz. Nauk **169**, 361 (1999).
9. J. L. Finney, J. Comput. Phys. **32**, 137 (1979).

Translated by V. Sakun

JETP Letters, Vol. 76, No. 2, 2002, pp. 107–111. Translated from Pis'ma v Zhurnal Éksperimental'noĭ i Teoreticheskoĭ Fiziki, Vol. 76, No. 2, 2002, pp. 118–122.

Effect of Elastic Deformations on the Multicritical Behavior of Disordered Systems

S. V. Belim

Omsk State University, Omsk, 644077 Russia

e-mail: belim@univer.omsk.su

Received May 23, 2002; in final form, June 13, 2002

Abstract—A field-theoretical description of the behavior of disordered, elastically isotropic, compressible systems characterized by two order parameters at the bicritical and tetracritical points is presented. The description is performed in the two-loop approximation in three dimensions with the use of the Padé–Borel summation technique. The renormalization group equations are analyzed, and the fixed points corresponding to different types of multicritical behavior are determined. It is shown that the effect of elastic deformations causes a change in the regime of the tetracritical behavior of disordered systems because of the interaction of the order parameters through the deformation field. © *2002 MAIK "Nauka/Interperiodica".*

PACS numbers: 64.60.Kw; 64.60.Ak; 61.43.Bn

It has been shown in [1] that the presence of frozen structural point defects gives rise to changes in the behavior of a system in both bicritical and tetracritical regions. According to the cited paper, the effect of δ-correlated impurities is essential only for Ising systems and leads to a decoupling of the order parameters at the multicritical points. Later [2], it was shown that elastic deformations cause a renormalization of the effective charges for the interaction of critical fluctuations, which lead to an increase in the interaction of order parameters and to a change in the type of multicritical behavior. Therefore, the study of the combined effect of elastic deformations and structural point defects in the multicritical region is of great interest.

The purpose of this paper is to study the influence of striction effects on disordered systems whose phase diagrams already contain multicritical points of bicritical or tetracritical type. In the first case, a multicritical point is the point of intersection of two lines of second-order phase transitions and one line of first-order phase transitions, while in the second case, it corresponds to the intersection of four lines of second-order phase transitions. In the immediate vicinity of a multicritical point, the system exhibits a specific critical behavior characterized by the competition between the types of ordering. At a bicritical point, one parameter is displaced by another, whereas the tetracritical point allows a mixed phase with a coexistence of different types of ordering. Such systems [1] can be described by introducing two order parameters that belong to different irreducible representations.

In structural phase transitions that occur in the absence of piezoelectric effect, in the paraphase, elastic strains play the role of a secondary order parameter whose fluctuations are not critical in most cases [3, 4]. Since, in the critical region, the main contribution to the striction effects comes from the dependence of the exchange integral on distance, only elastically isotropic systems are considered below.

The model Hamiltonian of a system has the form

$$
\begin{aligned}
H_0 = \int d^D x \Bigg[& \frac{1}{2}(\tau_1 + \nabla^2) \sum_{a=1}^{m} \Phi^a(x)^2 \\
& + \frac{1}{2}(\tau_1 + \nabla^2) \sum_{a=1}^{m} \Psi^a(x)^2 + \frac{u_{01}}{4!} \sum_{a,b=1}^{m} \Phi^a(x)^2 \Phi^b(x)^2 \\
& + \frac{u_{02}}{4!} \sum_{a,b=1}^{m} \Psi^a(x)^2 \Psi^b(x)^2 + \frac{2u_{03}}{4!} \sum_{a,b=1}^{m} (\Phi^a(x)\Psi^b(x))^2 \\
& - \frac{\delta_{01}}{2} \sum_{a=1}^{m} \Phi^a(x)^4 - \frac{\delta_{02}}{2} \sum_{a=1}^{m} \Psi^a(x)^4 \\
& - \delta_{03} \sum_{a=1}^{m} \Phi^a(x)^2 \Psi^a(x)^2 + g_1 y(x) \sum_{a=1}^{m} \Phi^a(x)^2 \\
& + g_2 y(x) \sum_{a=1}^{m} \Psi^a(x)^2 + \beta y(x)^2 \Bigg].
\end{aligned}
\tag{1}
$$

Here, $\Phi(x)$ and $\Psi(x)$ are the fluctuating order parameters; u_{01} and u_{02} are positive constants; $\tau_1 \sim |T - T_{c1}|/T_{c1}$ and $\tau_2 \sim |T - T_{c2}|/T_{c2}$, where T_{c1} and T_{c2} are the phase-transition temperatures for the first- and second-order parameters, respectively; $y(x) = \sum_{\alpha=1}^{3} u_{\alpha\alpha}(x)$, where $u_{\alpha\beta}$ is the strain tensor; g_1 and g_2 are the quadratic stric-

tion parameters; β is a constant characterizing the elastic properties of the crystal; and D is the space dimension. In this Hamiltonian, the integration with respect to the components depending on the nonfluctuating variables, which do not interact with the order parameters, is already performed along with the replica procedure of averaging over impurities. The properties of the initial system can be obtained in the limit $m \longrightarrow 0$. The nonnegative constants δ_{01}, δ_{02}, and δ_{03} describe the interaction of critical fluctuations via the impurity field. The interaction of impurities with elastic deformations has a linear character and, in the case of averaging over impurities, leads to the redetermination of the constants δ_{01}, δ_{02}, and δ_{03} [5].

By going to the Fourier transforms of the variables in Eq. (1), we obtain the Hamiltonian of the system in the form

$$
\begin{aligned}
H_0 &= \frac{1}{2}\int d^D q(\tau_1 + q^2)\sum_{a=1}^{m}\Phi_q^a\Phi_{-q}^a \\
&+ \frac{1}{2}\int d^D q(\tau_2 + q^2)\sum_{a=1}^{m}\Psi_q^a\Psi_{-q}^a \\
&+ \frac{u_{01}}{4!}\int d^D q_i \sum_{a,b=1}^{m}(\Phi_{q1}^a\Phi_{q2}^a)(\Phi_{q3}^b\Phi_{-q1-q2-q3}^b) \\
&+ \frac{u_{02}}{4!}\int d^D q_i \sum_{a,b=1}^{m}(\Psi_{q1}^a\Psi_{q2}^a)(\Psi_{q3}^b\Psi_{-q1-q2-q3}^b) \\
&+ \frac{2u_{03}}{4!}\int d^D q_i \sum_{a,b=1}^{m}(\Phi_{q1}^a\Phi_{q2}^a)(\Psi_{q3}^b\Psi_{-q1-q2-q3}^b) \\
&- \frac{\delta_{01}}{2}\int d^D q_i \sum_{a=1}^{m}(\Phi_{q1}^a\Phi_{q2}^a)(\Phi_{q3}^a\Phi_{-q1-q2-q3}^a) \\
&- \frac{\delta_{02}}{2}\int d^D q_i \sum_{a=1}^{m}(\Psi_{q1}^a\Psi_{q2}^a)(\Psi_{q3}^a\Psi_{-q1-q2-q3}^a) \\
&- \delta_{03}\int d^D q_i \sum_{a=1}^{m}(\Phi_{q1}^a\Phi_{q2}^a)(\Psi_{q3}^a\Psi_{-q1-q2-q3}^a) \\
&+ g_1\int d^D q y_{q1}\sum_{a=1}^{m}\Phi_{q2}^a\Phi_{-q1-q2}^a \\
&+ g_2\int d^D q y_{q1}\sum_{a=1}^{m}\Psi_{q2}^a\Psi_{-q1-q2}^a \\
&+ \frac{g_1^0}{\Omega}y_0\int d^D q\sum_{a=1}^{m}\Phi_q^a\Phi_{-q}^a + \frac{g_2^0}{\Omega}y_0\int d^D q\sum_{a=1}^{m}\Psi_q^a\Psi_{-q}^a \\
&+ 2\beta\int d^D q y_q y_{-q} + 2\frac{\beta_0}{\Omega}y_0^2.
\end{aligned}
\tag{2}
$$

Here, the components y_0 describing uniform strains are separated. According to [3], such a separation is necessary, because the nonuniform strains y_q are responsible for the exchange of acoustic phonons and lead to long-range interactions, which are absent in the case of uniform deformations.

We define the effective Hamiltonian that depends only on the strongly fluctuating order parameters Φ and Ψ of the system as follows:

$$
\begin{aligned}
&\exp\{-H[\Phi,\Psi]\} \\
&= B\int\exp\{-H_0[\Phi,\Psi,y]\}\prod dy_q.
\end{aligned}
\tag{3}
$$

If the experiment is performed at a constant volume, the quantity y_0 is a constant, and the integration in Eq. (3) is performed with respect to only the nonuniform strains, while the uniform strains do not contribute to the effective Hamiltonian. In an experiment at a constant pressure, the term $P\Omega$ is added to the Hamiltonian, with the volume being represented in terms of the strain tensor components in the form

$$
\Omega = \Omega_0\left[1 + \sum_{\alpha=1}u_{\alpha\alpha} + \sum_{\alpha\neq\beta}u_{\alpha\alpha}u_{\beta\beta} + O(u^3)\right], \tag{4}
$$

and the integration in Eq. (3) is performed also with respect to the uniform strains. According to [6], the inclusion of quadratic terms in Eq. (4) may be important at high pressures and for crystals with strong striction effects. As a result, we obtain

$$
\begin{aligned}
H &= \frac{1}{2}\int d^D q(\tau_1 + q^2)\sum_{a=1}^{m}\Phi_q^a\Phi_{-q}^a \\
&+ \frac{1}{2}\int d^D q(\tau_2 + q^2)\sum_{a=1}^{m}\Psi_q^a\Psi_{-q}^a \\
&+ \frac{v_{01}}{4!}\int d^D q_i \sum_{a,b=1}^{m}(\Phi_{q1}^a\Phi_{q2}^a)(\Phi_{q3}^b\Phi_{-q1-q2-q3}^b) \\
&+ \frac{v_{02}}{4!}\int d^D q_i \sum_{a,b=1}^{m}(\Psi_{q1}^a\Psi_{q2}^a)(\Psi_{q3}^b\Psi_{-q1-q2-q3}^b) \\
&+ \frac{2v_{03}}{4!}\int d^D q_i \sum_{a,b=1}^{m}(\Phi_{q1}^a\Phi_{q2}^a)(\Psi_{q3}^b\Psi_{-q1-q2-q3}^b) \\
&- \frac{\delta_{01}}{2}\int d^D q_i \sum_{a=1}^{m}(\Phi_{q1}^a\Phi_{q2}^a)(\Phi_{q3}^a\Phi_{-q1-q2-q3}^a)
\end{aligned}
$$

$$
\begin{aligned}
&-\frac{\delta_{02}}{2}\int d^D q_i \sum_{a=1}^{m} (\Psi^a_{q1}\Psi^a_{q2})(\Psi^a_{q3}\Psi^a_{-q1-q2-q3}) \\
&-\delta_{03}\int d^D q_i \sum_{a=1}^{m} (\Phi^a_{q1}\Phi^a_{q2})(\Psi^a_{q3}\Psi^a_{-q1-q2-q3}) \\
&+\frac{z_1^2-w_1^2}{2}\int d^D q_i \sum_{a,b=1}^{m} (\Phi^a_{q1}\Phi^a_{-q1})(\Phi^b_{q2}\Phi^b_{-q2}) \\
&+\frac{z_2^2-w_2^2}{2}\int d^D q_i \sum_{a=1}^{m} (\Psi^a_{q1}\Psi^a_{-q1})(\Psi^b_{q2}\Psi^b_{-q2}) \\
&+(z_1 z_2 - w_1 w_2)\int d^D q_i \sum_{a,b=1}^{m} (\Phi^a_{q1}\Phi^a_{-q1})(\Psi^b_{q2}\Psi^b_{-q2}),
\end{aligned}
\tag{5}
$$

$$v_{01} = u_{01} - 12z_1^2, \quad v_{02} = u_{02} - 12z_2^2,$$

$$v_{03} = u_{03} - 12z_1 z_2,$$

$$z_1 = \frac{g_1}{\sqrt{\beta}}, \quad z_2 = \frac{g_2}{\sqrt{\beta}}, \quad w_1 = \frac{g_1^0}{\sqrt{\beta_0}}, \quad w_2 = \frac{g_2^0}{\sqrt{\beta_0}}.$$

This Hamiltonian leads to a wide variety of multicritical points. As for incompressible systems, both tetracritical

$$(v_3 + 12(z_1 z_2 - w_1 w_2 - \delta_3))^2 < (v_1 + 12(z_1^2 - w_1^2 - \delta_1))(v_2 + 12(z_2^2 - w_2^2 - \delta_2))$$

and bicritical

$$(v_3 + 12(z_1 z_2 - w_1 w_2 - \delta_3))^2 > (v_1 + 12(z_1^2 - w_1^2 - \delta_1))(v_2 + 12(z_2^2 - w_2^2 - \delta_2))$$

behaviors are possible. In addition, the striction effects may give rise to multicritical points of higher orders.

In the framework of the field-theoretical approach [7], the asymptotic critical behavior and the structure of the phase diagram in the fluctuation region are determined by the Callan–Symanzik renormalization-group equation for the vertex parts of the irreducible Green's functions. To calculate the β and γ functions as functions involved in the Callan–Symanzik equation for renormalized interaction vertices u_1, u_2, u_3, δ_1, δ_2, δ_3, g_1, g_2, $g_1^{(0)}$, and $g_2^{(0)}$ or for complex vertices z_1, z_2, w_1, w_2, v_1, v_2, v_3, δ_1, δ_2, and δ_3, which are more convenient for the determination of the multicritical behavior, the standard method based on the Feynman diagram technique and on the renormalization procedure was used [8]. As a result, the following expressions were obtained for the β functions in the two-loop approximation:

$$
\begin{aligned}
\beta_{v1} &= -v_1 + \frac{3}{2}v_1^2 + \frac{1}{6}v_3^2 - 24v_1\delta_1 - \frac{77}{81}v_1^3 \\
&- \frac{23}{243}v_1 v_3^2 - \frac{2}{27}v_3^3 + \frac{184}{81}v_1 v_3\delta_3 + \frac{16}{9}v_3^2\delta_3 \\
&+ \frac{832}{27}v_1^2\delta_1 - \frac{5920}{27}v_1\delta_1^2 + \frac{8}{9}v_3^2\delta_1,
\end{aligned}
$$

$$
\begin{aligned}
\beta_{v2} &= -v_2 + \frac{3}{2}v_2^2 + \frac{1}{6}v_3^2 - 24v_2\delta_1 - \frac{77}{81}v_2^3 \\
&- \frac{23}{243}v_2 v_3^2 - \frac{2}{27}v_3^3 + \frac{184}{81}v_2 v_3\delta_3 + \frac{16}{9}v_3^2\delta_3 \\
&+ \frac{832}{27}v_2^2\delta_2 - \frac{5920}{27}v_2\delta_2^2 + \frac{8}{9}v_3^2\delta_2,
\end{aligned}
$$

$$
\begin{aligned}
\beta_{v3} &= -v_3 + \frac{2}{3}v_3^2 + \frac{1}{2}v_1 v_3 + \frac{1}{2}v_2 v_3 - 4v_3\delta_1 \\
&- 4v_3\delta_2 - 16v_3\delta_3 - \frac{41}{243}v_3^3 - \frac{23}{162}v_1^2 v_3 \\
&- \frac{23}{162}v_2^2 v_3 - \frac{1}{3}v_1 v_3^2 - \frac{1}{3}v_2 v_3^2 + \frac{472}{81}v_3^2\delta_3 \\
&+ \frac{8}{3}v_3^2\delta_1 + \frac{8}{3}v_3^2\delta_2 - \frac{368}{27}v_3\delta_1^2 - \frac{368}{27}v_3\delta_2^2 \\
&+ \frac{92}{27}v_1 v_3\delta_1 + \frac{92}{27}v_2 v_3\delta_2 + 8v_1 v_3\delta_3 + 8v_2 v_3\delta_3 \\
&- 64v_3\delta_3^2 - 64v_3\delta_1\delta_3 - 64v_3\delta_2\delta_3,
\end{aligned}
$$

$$
\begin{aligned}
\beta_{\delta1} &= -\delta_1 + 16\delta_1^2 - v_1\delta_1 - \frac{1}{3}v_3\delta_3 - \frac{3040}{27}\delta_1^3 \\
&+ \frac{2}{27}v_3^2\delta_3 - \frac{8}{3}v_3\delta_3^2 - \frac{400}{27}v_1\delta_1^2 + \frac{23}{81}v_1^2\delta_1 \\
&+ \frac{5}{243}v_3^2\delta_1 - \frac{184}{81}v_3\delta_1\delta_3,
\end{aligned}
$$

$$
\begin{aligned}
\beta_{\delta2} &= -\delta_2 + 16\delta_2^2 - v_1\delta_2 - \frac{1}{3}v_3\delta_3 - \frac{3040}{27}\delta_2^3 \\
&+ \frac{2}{27}v_3^2\delta_3 - \frac{8}{3}v_3\delta_3^2 - \frac{400}{27}v_2\delta_2^2 + \frac{23}{81}v_2^2\delta_2 \\
&+ \frac{5}{243}v_3^2\delta_2 - \frac{184}{81}v_3\delta_2\delta_3,
\end{aligned}
$$

$$
\begin{aligned}
\beta_{\delta3} &= -\delta_3 + 8\delta_3^2 + \frac{1}{2}v_1\delta_3 + \frac{1}{2}v_2\delta_3 + \frac{1}{6}v_3\delta_1 \\
&+ \frac{1}{6}v_3\delta_2 + 4\delta_1\delta_3 + 4\delta_2\delta_3 - \frac{64}{3}\delta_3^3 + 4v_1\delta_3^2
\end{aligned}
$$

$$+4v_2\delta_3^2+\frac{23}{162}v_1^2\delta_3+\frac{23}{162}v_2^2\delta_3+\frac{368}{27}\delta_1^2\delta_3 \quad (6)$$

$$+\frac{368}{27}\delta_2^2\delta_3+32\delta_1\delta_3^2+32\delta_2\delta_3^2+\frac{1}{27}v_3^2\delta_1$$

$$+\frac{1}{27}v_3^2\delta_2-\frac{4}{9}v_3\delta_1^2-\frac{4}{9}v_3\delta_2^2+\frac{5}{243}v_3^2\delta_3$$

$$-\frac{40}{81}v_3\delta_3^2-\frac{92}{27}v_1\delta_1\delta_3-\frac{92}{27}v_2\delta_2\delta_3$$

$$-\frac{16}{9}v_3\delta_1\delta_3-\frac{16}{9}v_3\delta_2\delta_3,$$

$$\beta_{z1}=-z_1+v_1z_1+2z_1^3-16\delta_1z_1-4\delta_3z_2$$

$$+2z_1z_2^2+\frac{1}{3}v_3z_2-\frac{23}{81}v_1^2z_1-\frac{7}{243}v_3^2z_1-\frac{2}{27}v_3^2z_2$$

$$+\frac{29}{27}v_1z_1\delta_1-\frac{736}{27}z_1\delta_1^2-\frac{16}{3}z_1\delta_3^2-\frac{32}{3}z_2\delta_3^2$$

$$+\frac{512}{27}v_3z_1\delta_3+\frac{512}{27}v_3z_2\delta_3,$$

$$\beta_{z2}=-z_2+v_2z_2+2z_2^3-16\delta_2z_2-4\delta_3z_1$$

$$+2z_2z_1^2+\frac{1}{3}v_3z_1-\frac{23}{81}v_2^2z_2-\frac{7}{243}v_3^2z_2-\frac{2}{27}v_3^2z_1$$

$$+\frac{29}{27}v_2z_2\delta_2-\frac{736}{27}z_2\delta_2^2-\frac{16}{3}z_2\delta_3^2$$

$$-\frac{32}{3}z_1\delta_3^2+\frac{512}{27}v_3z_2\delta_3+\frac{512}{27}v_3z_1\delta_3,$$

$$\beta_{w1}=-w_1+v_1w_1+2z_1^2w_1-2w_1^3-16\delta_1w_1$$

$$-4\delta_3w_2+2w_1z_2^2+\frac{1}{3}v_3w_2-\frac{23}{81}v_1^2w_1$$

$$-\frac{7}{243}v_3^2w_1-\frac{2}{27}v_3^2w_2+\frac{29}{27}v_1w_1\delta_1-\frac{736}{27}w_1\delta_1^2$$

$$-\frac{16}{3}w_1\delta_3^2-\frac{32}{3}w_2\delta_3^2+\frac{512}{27}v_3w_1\delta_3+\frac{512}{27}v_3w_2\delta_3,$$

$$\beta_{w2}=-w_2+v_2w_2+2z_2^2w_2-2w_2^3-16\delta_2w_2$$

$$-4\delta_3w_1+2w_2z_1^2+\frac{1}{3}v_3w_1-\frac{23}{81}v_2^2w_2$$

$$-\frac{7}{243}v_3^2w_2-\frac{2}{27}v_3^2w_1+\frac{29}{27}v_2w_2\delta_2-\frac{736}{27}w_2\delta_2^2$$

$$-\frac{16}{3}w_2\delta_3^2-\frac{32}{3}w_1\delta_3^2+\frac{512}{27}v_3w_2\delta_3+\frac{512}{27}v_3w_2\delta_3.$$

It is well known that the perturbative series expansions are asymptotic, and the vertices of the interactions of the order parameter fluctuations in the fluctuation region are sufficiently large for Eqs. (6) to be directly applied. Therefore, to extract the necessary physical information from the expressions derived above, the Padé–Borel method generalized to the multiparameter case was used. The corresponding direct and inverse Borel transformations have the form

$$f(v_1, v_2, v_3, \delta_1, \delta_2, \delta_3, z_1, z_2, w_1, w_2)$$

$$=\sum_{i_1,\ldots,i_{10}} c_{i_1\ldots i_{10}} v_1^{i_1}v_2^{i_2}v_3^{i_3}\delta_1^{i_4}\delta_2^{i_5}\delta_3^{i_6}z_1^{i_7}z_2^{i_8}w_1^{i_9}w_2^{i_{10}} \quad (7)$$

$$=\int_0^\infty e^{-t}F(v_1t, v_2t, v_3t, \delta_1t, \delta_2t, \delta_3t, z_1t, z_2t, w_1t, w_2t)dt,$$

$$F(v_1, v_2, v_3, \delta_1, \delta_2, \delta_3, z_1, z_2, w_1, w_2)$$

$$=\sum_{i_1,\ldots,i_{10}} \frac{c_{i_1\ldots i_7}}{(i_1+\ldots+i_{10})!} v_1^{i_1}v_2^{i_2}v_3^{i_3}\delta_1^{i_4}\delta_2^{i_5}\delta_3^{i_6}z_1^{i_7}z_2^{i_8}w_1^{i_9}w_2^{i_{10}}. \quad (8)$$

For an analytic continuation of the Borel transform of a function, a series in an auxiliary variable θ is introduced:

$$\tilde{F}(v_1, v_2, v_3, \delta_1, \delta_2, \delta_3, z_1, z_2, w_1, w_2, \theta)$$

$$=\sum_{k=0}^\infty \theta^k \sum_{i_1,\ldots,i_{10}} \frac{c_{i_1\ldots i_{10}}}{k!} \quad (9)$$

$$\times v_1^{i_1}v_2^{i_2}v_3^{i_3}\delta_1^{i_4}\delta_2^{i_5}\delta_3^{i_6}z_1^{i_7}z_2^{i_8}w_1^{i_9}w_2^{i_{10}}\delta_{i_1+\ldots+i_{10},k},$$

and the $[L/M]$ Padé approximation is applied to this series at the point $\theta = 1$. This approach was proposed and tested in [9] for describing the critical behavior of systems characterized by several vertices corresponding to the interaction of the order parameter fluctuations. The property [9] that the system retains its symmetry under the Padé approximants in the variable θ is essential in the description of multivertex models.

In the two-loop approximation, the β functions were calculated using the [2/1] approximant. The character of the critical behavior is determined by the existence of a stable fixed point satisfying the set of equations

$$\beta_i(v_1^*, v_2^*, v_3^*, \delta_1^*, \delta_2^*, \delta_3^*, z_1^*, z_2^*, w_1^*, w_1^*) = 0 \quad (i = 1, \ldots, 10). \quad (10)$$

The requirement that the fixed point be stable is reduced to the condition that the eigenvalues b_i of the matrix

$$B_{i,j}=\frac{\partial\beta_i(v_1^*, v_2^*, v_3^*, \delta_1^*, \delta_2^*, \delta_3^*, z_1^*, z_2^*, w_1^*, w_1^*)}{\partial v_j} \quad (11)$$

$$(v_i, v_j \equiv v_1^*, v_2^*, v_3^*, \delta_1^*, \delta_2^*, \delta_3^*, z_1^*, z_2^*, w_1^*, w_1^*)$$

lie on the right-hand complex half-plane.

The resulting set of summed β functions contains a wide variety of fixed points lying in the physical region of the vertex values with $v_i \geq 0$.

A complete analysis of the fixed points, each of which corresponds to the critical behavior of a single order parameter, was presented in our recent publication [5]. Now, we consider the combined critical behavior of two order parameters.

The analysis of the values and stability of the fixed points offers a number of conclusions. The tetracritical fixed point of a disordered incompressible system ($v_1 = v_2 = 1.58892$, $v_3 = 0$, $\delta_1 = \delta_2 = 0.03448$, $\delta_3 = 0$, $z_1 = 0$, $z_2 = 0$, $w_1 = 0$, $w_2 = 0$) is unstable under the effect of uniform deformations ($b_1 = b_2 = 0.461$, $b_3 = 0.036$, $b_4 = b_5 = 0.461$, $b_6 = 0.036$, $b_7 = b_8 = b_9 = b_{10} = -0.236$). The striction effects lead to the stabilization of the tetracritical fixed point of a compressible disordered system ($v_1 = v_2 = 1.58892$, $v_3 = 0$, $\delta_1 = \delta_2 = 0.03448$, $\delta_3 = 0$, $z_1 = 0.04599$, $z_2 = 0.568836$, $w_1 = 0.017759$, $w_2 = 0.551849$, $b_1 = b_2 = 0.461$, $b_3 = 0.036$, $b_4 = b_5 = 0.461$, $b_6 = 0.036$, $b_7 = 1.189$, $b_8 = 0.003$, $b_9 = 5.391$, $b_{10} = 0.999$).

The question about the stability of other multicritical points cannot be resolved in terms of the described model, because the calculations lead to a degenerate set of equations. The degeneracy can be removed by considering the Hamiltonian with allowance for the terms of higher orders in both the strain tensor components and the fluctuating order parameters.

Thus, the striction-induced interaction of the fluctuating order parameters with elastic deformations, as well as the introduction of frozen point impurities into the system, leads to a change from the bicritical behavior to the tetracritical one. Elastic deformations lead to a change in the regime of tetracritical behavior of a disordered system because of the interaction between the order parameters through the acoustic phonon exchange.

REFERENCES

1. V. V. Prudnikov, P. V. Prudnikov, and A. A. Fedorenko, Fiz. Tverd. Tela (St. Petersburg) **42**, 158 (2000) [Phys. Solid State **42**, 165 (2000)].
2. S. V. Belim, Pis'ma Zh. Éksp. Teor. Fiz. **75**, 547 (2002) [JETP Lett. **75**, 457 (2002)].
3. A. I. Larkin and S. A. Pikin, Zh. Éksp. Teor. Fiz. **56**, 1664 (1969) [Sov. Phys. JETP **29**, 891 (1969)].
4. Y. Imry, Phys. Rev. Lett. **33**, 1304 (1974).
5. S. V. Belim and V. V. Prudnikov, Fiz. Tverd. Tela (St. Petersburg) **45**, 1299 (2001) [Phys. Solid State **43**, 1353 (2001)].
6. D. J. Bergman and B. I. Halperin, Phys. Rev. B **13**, 2145 (1976).
7. D. J. Amit, *Field Theory, the Renormalization Group, and Critical Phenomena* (McGraw-Hill, New York, 1976).
8. J. Zinn-Justin, *Quantum Field Theory and Critical Phenomena* (Clarendon, Oxford, 1989).
9. S. A. Antonenko and A. I. Sokolov, Phys. Rev. B **49**, 15901 (1994); K. B. Varnashev and A. I. Sokolov, Fiz. Tverd. Tela (St. Petersburg) **38**, 3665 (1996) [Phys. Solid State **38**, 1996 (1996)]; A. I. Sokolov, K. B. Varnashev, and A. I. Mudrov, Int. J. Mod. Phys. B **12**, 1365 (1998); A. I. Sokolov and K. B. Varnashev, Phys. Rev. B **59**, 8363 (1999).

Translated by E. Golyamina

JETP Letters, Vol. 76, No. 2, 2002, pp. 112–114. Translated from Pis'ma v Zhurnal Éksperimental'noĭ i Teoreticheskoĭ Fiziki, Vol. 76, No. 2, 2002, pp. 123–125.

Quasi-Hexagonal Self-Organization of Nanoparticles upon the Laser-Controlled Deposition of Ga Atoms

V. I. Emel'yanov*, K. I. Eremin*, and N. I. Zheludev**

** International Laser Center, Moscow State University, Moscow, 119899 Russia*

*** University of Southampton, Southampton, SO17, Great Britain*

e-mail:emel@em.msk.ru

Received June 20, 2002

Abstract—A cooperative defect–deformation (DD) mechanism is developed for the nucleation of the quasi-monodisperse ensemble of nanoparticles in the low-temperature deposition of Ga atoms in the presence of laser radiation. A comparison with experiment is carried out, and a good agreement between the theoretical and experimental results has been obtained. In particular, in accordance with the DD model, it has been found that the arrangement of nanoparticles is characterized by a latent hexagonal order, and their shape is quasi-hexagonal. It has been shown that the characteristics of the deposited ensemble of nanoparticles can be controlled with the use of an anisotropic deformation. © *2002 MAIK "Nauka/Interperiodica".*

PACS numbers: 81.16.Rf, 81.16.Mk

1. In recent years, the spontaneous formation of periodic nanostructures of adatoms on crystal surfaces has become a subject of intensive studies [1]. Recently, the formation of a virtually close-packed arrangement of Ga nanoparticles (Fig. 1a) with a narrow size distribution was observed in [2]. The nanostructure was generated on the illuminated part of the end of a silica optical fiber (in its core) upon the molecular-beam deposition of Ga atoms. The optical-fiber temperature was maintained at $T = 100$ K. Ga particles with a broad size distribution were formed in the part of the end where laser radiation was absent (Fig. 1b).

In this work, based on the defect–deformation theory of the formation of periodic adatom structures with the participation of a surface quasi-Rayleigh acoustic wave [3], a DD mechanism is developed for the cooperative space-periodic nucleation of nanoparticles induced by laser radiation. A two-dimensional Fourier transformation of an AFM scan of the optical-fiber end surface made after deposition has revealed a quasi-hexagonal order in the arrangement of gallium nanoparticles, which confirms one of the main predictions of the DD mechanism. It has been found that the spatial distribution of nanoparticles can be controlled with the use of an anisotropic external deformation breaking the symmetry of the diffusion of adatoms over the surface in the process of the DD self-organization of an ensemble of nanoparticles.

2. In the experiment [2], a beam of Ga atoms is incident on the end of an optical fiber with laser radiation introduced into it. Ga atoms are adsorbed on the end surface and then become bound by a covalent bond in pairs, forming dimers analogous to the dimers in the α-Ga crystal [4]. The absorption of an $\hbar\omega$ radiation quantum with a wavelength of 1550 nm [2], which lies inside the molecular absorption band of Ga dimers [4], transfers the dimer from the ground state to an excited state. Relaxation from the excited state to the ground one proceeds through radiationless transitions with the liberation of energy $\lesssim\hbar\omega$. This energy decreases the activation energy of the surface diffusion of a dimer: $E \longrightarrow E - \hbar\omega$, where E is the equilibrium activation energy of diffusion. In this case, the diffusion coefficient $D_d = D_0\exp(-(E - \hbar\omega)/kT)$ increases so that the diffusion of dimers in the illuminated area of the optical-fiber end occurs even at low temperatures. At the same time, the activation energy in the unilluminated area of the optical-fiber end (outside its core) remains large, the diffusion coefficient remains respectively small, and the diffusion of dimers does not occur.

3. The mobile dimers can be considered as mobile defects on the surface (surface elastic inclusions). Because of the deformation potential of a surface dimer and the local renormalization of the surface energy, the dimers nonuniformly deform the surface and the underlying elastic continuum. In its turn, the resulting nonuniform self-consistent surface deformation redistributes the dimers over the surface through the defect deformation potential as well. It is shown in [3] that such a DD feedback leads to the development of DD instability. With this instability, two coupled gratings are built up in time with an growth rate λ: the surface deformation grating $\xi = \xi(q)\exp(iqx + \lambda t)$ and the adatom (dimer) concentration grating $N_d = N_d(q)\exp(iqx + \lambda t)$, where the coordinate x is reckoned along a certain preferred direction on the surface. The DD instability growth rate in the limit of a relatively small surface energy modulation takes the form [3] $\lambda(q) =$

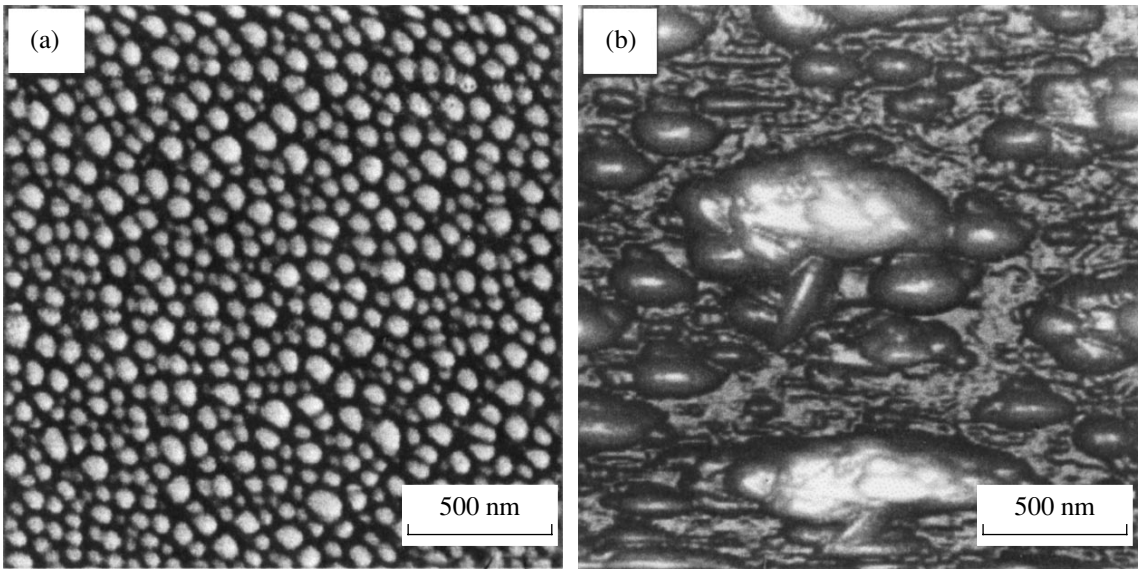

Fig. 1. AFM scan of the optical fiber surface after the deposition of Ga atoms during 30 min with a rate of ~0.3 nm/min: (a) illuminated area of the optical fiber (pulsed laser radiation with a pulse duration of 1 μs, a repetition rate of 1 kHz, and the peak power F = 17 mW); (b) unilluminated area of the optical fiber (by the results of [2]).

$D_d q^2[(N_{d0}/N_{dc})(1 - l_d^2 q^2) - 1]$. Here, the critical dimer concentration $N_{dc} = (1 - \beta)(a\rho c_l^2 kT/\theta_d^2)$; $\beta = c_t^2/c_l^2$ and c_l and c_t are, respectively, the longitudinal and transverse velocities of sound; ρ is the medium density; a is the surface lattice constant; θ_d is the surface dimer deformation potential; l_d is the characteristic length of the dimer interaction with grating atoms, which lies in the nanometer range and determines the screening length of the elastic interaction between dimers [5]. At θ_d = 10 eV, T = 100 K, $a = 5 \times 10^{-8}$ cm, and $\rho c_l^2 = 1 \times 10^2$ erg/cm^3, we obtain $N_{dc} \approx 1.8 \times 10^{12}$ cm^{-2}.

The function $\lambda(q)$ has a maximum at the value of the wave number $q = q_m$, which determines the period $\Lambda = 2\pi/q_m$ of the dominating DD grating: $\Lambda(N_{d0}) = \sqrt{8}\,\pi l_d[1 - N_{dc}/N_{d0}]^{-1/2}$. The formation of the DD grating on the surface proceeds in a threshold way on exceeding the critical dimer concentration $N_{d0} > N_{dc}$. At a constant dimer concentration N_{d0} = const, the period is determined by the temperature $\Lambda(T) = \sqrt{8}\,\pi l_d[1 - T_0/T_c]^{-1/2}$, where the critical temperature $T_c = \theta_d^2 N_{d0}/(1 - \beta)a\rho c_l^2 k \sim 110$ K (at $N_{d0} = 2 \times 10^{12}$ cm^{-2}). The DD grating can form on the surface only at $T < T_c$.

4. The periodic surface deformation field arising on the formation of the DD grating generates fluxes of mobile Ga clusters nucleated in a random way. These fluxes are directed toward the extrema of the deformation. By virtue of this fact, only those clusters grow that reside at the extrema of the surface deformation field. Thus, after a certain time interval of growth, a close-packed arrangement of nanoparticles with a narrow size distribution forms in the illuminated surface area. This distribution is centered at a value proportional to the period Λ of the DD nanostructure. As follows from the given consideration, the nucleation of the DD nanostructure can proceed only at $T < T_c$. This condition agrees with the results obtained in [2], where the nanostructuring of Ga was observed at T = 100 K and was absent at T = 300 K. In the area where there is no light, the deposition products are of low mobility at low temperatures, and the DD instability cannot occur. In this area, particles nucleate in a random way, and their growth also proceeds randomly. As a result, particles with a broad size distribution form in the unilluminated area (Fig. 1b).

5. The direction x becomes preferred on the isotropic surface as a result of the spontaneous breaking of the DD system symmetry. It is likely that, because of nonlinear pair interactions between the DD gratings, the dominating structure will be a superposition of three DD gratings with wave vectors forming a regular triangle on the surface, that is, a hexagonal DD structure (similar to that obtained in [6, 7]). In this case, the absolute deformation extrema form a hexagonal cellular structure on the surface and can serve as nucleation centers of the cellular nanostructure of Ga clusters.

In order to verify the prediction of long-range hexagonal order in the arrangement of nanoparticles, we carried out a computer two-dimensional Fourier transformation of an AFM image of the surface after deposition (Fig. 1a). A smoothed amplitude part of the Fourier spectrum $|F(k_x, k_y)|$ is shown in Fig. 2. The most interesting feature of the spectrum is the occurrence of three

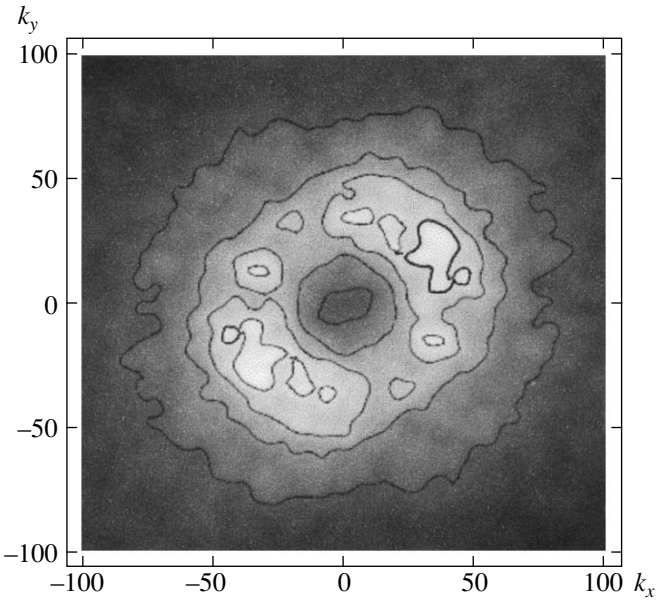

Fig. 2. Smoothed amplitude part $|F(k_x, k_y)|$ of the Fourier spectrum of the AFM image shown in Fig. 1a; k_x and k_y are dimensionless wave numbers. The actual wave numbers are $q_x = 2\pi k_x/L_x$ and $q_y = 2\pi k_y/L_y$, where $L_x = 2000$ nm and $L_y = 2000$ nm are actual dimensions of the scanned surface area. Brighter areas correspond to larger values of $|F(k_x, k_y)|$.

pairs of intense maxima (maxima of one of the pairs are split into doublets). Each pair, lying symmetrically with respect to the center of the ellipsoid on lines passing through its center, corresponds to the grating of the local surface brightness of the image, that is, to the grating of nanoparticles. Thus, the pattern observed in Fig. 1a is formed by three groups of nanoparticle gratings. Their wave vectors **q** are approximately equal to each other in magnitude and are directed at certain angles to each other, which corresponds to the occurrence of latent long-range quasi-hexagonal order in the arrangement of nanoparticles. It is evident in Fig. 2 that the maxima are located on a plateau, which has a quasi-hexagonal shape. Our computer simulation shows that the shape of nanoparticles is responsible for the shape of the plateau. Thus, the projection of nanoparticles onto the image plane has a quasi-hexagonal shape; that is, the nanoparticles tend to approach a hexagonal prism in shape (this can be seen in Fig. 1a).

The perfect hexagonal order in the case under consideration (Fig. 1a, 2) is disturbed for the following reasons. The nonuniformity of the cleavage surface and the deformation of the optical fiber (generated, for example, by its twisting) induce a surface strain. The uniaxial strain of a certain sign (tensile or compressive) increases the diffusion coefficient along its direction. Therefore, it "entraps" one of the DD gratings, orienting the grating vector along this direction, and makes this grating most intense. This DD selected by the strain corresponds to the pair of the most intense maxima in Fig. 2. On the contrary, a strain of the opposite sign (compressive or tensile) leads to the repulsion of the DD grating vectors from their direction. In addition, the computer analysis shows that the phase part of the Fourier spectrum $\arg(F(k_x, k_y))$ represents a function with randomly distributed values in the interval $[\pi, -\pi]$. Thus, three DD gratings have random phases, which also disturbs the long-range hexagonal order in the arrangement of nanoparticles.

The authors (VIE and NIZh) are grateful to the Engineering and Physical Sciences Research Council (EPSRC, Great Britain) for financial support, project no. RG/R4441538/01).

REFERENCES

1. V. A. Shchukin and D. Bimberg, Rev. Mod. Phys. **71**, 1125 (1999).
2. K. F. MacDonald, W. S. Brocklesby, V. I. Emel'yanov, *et al.*, Appl. Phys. Lett. **80**, 1643 (2002).
3. V. I. Emel'yanov and K. I. Eremin, Pis'ma Zh. Éksp. Teor. Fiz. **75**, 109 (2002) [JETP Lett. **75**, 98 (2002)].
4. X. G. Gong, G. L. Chiarrotti, M. Parinello, and E. Tosatti, Phys. Rev. B **43**, 14277 (1991).
5. V. I. Emel'yanov and I. M. Panin, Fiz. Tverd. Tela (St. Petersburg) **39**, 2029 (1997) [Phys. Solid State **39**, 1815 (1997)]; Fiz. Tverd. Tela (St. Petersburg) **42**, 1026 (2000) [Phys. Solid State **42**, 1058 (2000)]; Fiz. Tverd. Tela (St. Petersburg) **43**, 637 (2001) [Phys. Solid State **43**, 663 (2001)].
6. H. Haken, *Synergetics: An Introduction: Nonequilibrium Phase Transitions and Self-Organization in Physics, Chemistry, and Biology* (Springer, Berlin, 1977).
7. D. Walgraef, N. M. Ghoniem, and J. Lauzeral, Phys. Rev. B **56**, 15361 (1997).

Translated by A. Bagatur'yants

JETP Letters, Vol. 76, No. 2, 2002, pp. 77–79. From Pis'ma v Zhurnal Éksperimental'noĭ i Teoreticheskoĭ Fiziki, Vol. 76, No. 2, 2002, pp. 89–91.

Fundamental Constants in Effective Theory¶

G. E. Volovik

Low Temperature Laboratory, Helsinki University of Technology, FIN-02015 HUT, Finland
Landau Institute for Theoretical Physics, Russian Academy of Sciences, ul. Kosygina 2, Moscow, 117940 Russia

Received June 20, 2002

Abstract—In the discussion between L.B. Okun, G. Veneziano, and M.J. Duff concerning the number of fundamental dimensionful constants in physics [9], they advocated, respectively, 3, 2, and 0 fundamental constants. Here, we consider this problem with an example of effective relativistic quantum field theory, which emerges in the low-energy corner of quantum liquids and which reproduces many features of our physics, including Lorentz invariance, chiral fermions, gauge fields, and dynamical gravity. © *2002 MAIK "Nauka/Interperiodica".*

PACS numbers: 06.20.Jr; 04.90.+e; 11.90.+t; 67.90.+z

1. Introduction. Experimental bounds on the possible variation of fundamental constants in nature are discussed in comprehensive review [1]. Since we live well below Planck's energy scale, we cannot judge which of them are really fundamental, i.e., cannot be derived from the underlying trans-Planckian physics. Here, we discuss this problem using the effective relativistic quantum field theory (RQFT) arising as emergent phenomenon in quantum liquids [2] or in other condensed matter systems [3]. Since the trans-Planckian physics of a quantum liquid—microscopic atomic physics—is well known, at least, in principle, this allows us to look at the problem of fundamental constants from the outside, i.e., from the point of view of an external observer who does not belong to the low-energy world of the effective RQFT. This observer knows both effective and microscopic physics. He or she knows the origin of the "constants" which enter the effective theory and, thus, can judge whether they are fundamental within the effective theory and whether they remain fundamental at the more fundamental (i.e., more microscopic) level.

The status of fundamental constants in quantum liquids depends on the energy scale used: the low-energy scale, where the effective theory applies, or the atomic scale of the "Theory of Everything." Within the effective theory, the status of constants also depends on the observer who measures them: the "inner" observer belonging to the world of low-energy quasiparticles or the external observer who belongs to the world of microphysics. In table (1), we will use the following criteria for fundamentality. The first line shows whether the constant is (+) or is not (–) fundamental from the point of view of an inner observer. The constant is fundamental if it cannot be derived within the effective theory used by the inner observer. The second line refers to the external observer if he uses the effective theory only. For him, the fundamental constant is the phenomenological parameter. In the complete equilibrium of a quantum liquid and in the absence of external perturbations, this phenomenological parameter is completely fixed and, thus, can be considered as fundamental. Finally, the third line corresponds to the Weinberg criterion [4]: the constant is not fundamental if it can be derived from the parameters of microscopic physics.

In the table, we consider the status of the following constants: Planck's constant $\hbar$; the speed of light c, i.e., the maximum attainable velocity in the effective theory; and Newton's gravitational constant G. From 19 parameters of the Standard Model, we discuss only one, the fine-structure constant α, which has a direct analog in superfluid ^{3}He-A [2]:

constant	$\hbar$	G	c	α
effective theory–inner observer	+	+	+	–
effective theory–external observer	+	+	–	–
microphysics	+	–	–	–

Scheme 1.

Let us now discuss the status of each of the four constants.

2. Planck's constant $\hbar$. Inspection of the RQFT emerging in quantum liquids demonstrates that, within this scheme, we have only one fundamental constant, Planck's constant $\hbar$. It is fundamental both within the effective RQFT at low energy and in the microscopic physics of liquids [all signs in the $\hbar$ column of Scheme 1 are +]. Quantum mechanics is built in quantum liquids, which are essentially quantum objects. It is the quantum zero-point motion of atoms which gives rise to the ground state of the ^{3}He-A liquid, where the low-energy fermionic and bosonic collective modes behave as relativistic chiral fermions and gauge and gravitational fields. The limit $\hbar = 0$ simply does not

¶This article was submitted by the author in English.

exist, since there is no vacuum at $\hbar = 0$, and, thus, no effective theory.

In quantum liquids belonging to the same universality class of Fermi points as ^{3}He-A, almost all physical laws of our world are formed in the low-energy corner, except for quantum mechanics, which is present from the very beginning. In principle, it is not excluded that, in the more comprehensive systems, quantum mechanics will also acquire the status of an emergent low-energy phenomenon [5], with the minus sign in the third line of the $\hbar$ column. Since this does not happen in our quantum liquids, we have no solid basis for discussing the possibility of varying $\hbar$.

3. Speed of light. The metric of the effective "Minkowski" spacetime, in which the "relativistic" quasiparticles (fermions and bosons) propagate along the geodesic curves in anisotropic quantum liquids, has the following local structure: $g_{\mu\nu} = \mathrm{diag}(-1, c_x^{-2}, c_y^{-2}, c_z^{-2})$. The analog of the speed of light—the maximum attainable speed for low-energy fermions or/and bosons—depends on the direction of fermion or boson propagation. Since for an external observer there is no unique speed of light c, we have the minus sign in the second and third lines of the c column in Scheme 1.

The question that arises in the case of the anisotropic speed of light is, What "speed of light" enters the Einstein relation $M = mc^2$ between the rest energy and the mass of the object? More generally, Which c enters physical equations?

The answer to this question is rather simple: the speed of light c never explicitly enters any physically reasonable equation if it is written in the covariant and gauge-invariant form. The speed of light is hidden within the metric tensor, which is the relevant dynamical variable. For example, the above metric $g_{\mu\nu} = \mathrm{diag}(-1, c_x^{-2}, c_y^{-2}, c_z^{-2})$ enters the energy spectrum of a massive particle in the following way: $E^2 = M^2 + g^{ik}p_ip_k$ or $g^{\mu\nu}p_\mu p_\nu + M^2 = 0$, where M is the rest energy. In these equations, there is no c.

The mass is usually determined as the response of momentum to velocity: $p_i = M_{ik}v^k$. Since the velocity of a particle is $v_i = dE/dp_i$, one obtains for the mass tensor, $M_{ik} = Eg_{ik}$. If the linear response of the momentum to velocity is considered, one has

$$M_{ik}(\text{linear}) \equiv M_{ik}(\mathbf{v} = 0) = Mg_{ik}. \qquad (1)$$

This equation contains the rest energy M, but does not contain c and m explicitly. The same is true for any equation written in covariant form: it never contains m and c separately.

In the effective theory, the problem of the fundamentality of c is rather specific. For an inner observer living in the liquid, who uses the rods and clocks made from low-energy quasiparticles, the "speed of light" does not depend on the direction of propagation. Moreover, it does not depend on the velocity of the inner observer with respect to the liquid. This happens because of the physical Lorentz contraction experienced by his rods made of quasiparticles; his clocks made of quasiparticles experience the retardation of time. All this conspires the inner observer to believe that the speed of light is fundamental. Such a low-energy observer can safely divide the rest energy M by his c^2. He will obtain what he thinks is the mass of the object, and this belief will be shared by all the low-energy inner observers. In this sense, the speed of light is fundamental and the first line of Scheme 1 contains the plus sign.

However, for the external observer who lives outside the quantum liquid and uses the rigid rods and laboratory clocks in his experiments, the speed of massless quasiparticles is anisotropic even in the low-energy limit, i.e., in the range of applicability of the effective theory. He or she finds that, say, in ^{3}He-A the "speed of light" varies from 3 cm/s to 60 m/s depending on the direction. This means that, for the external observer, the speed of light is not fundamental both in the microscopic and effective theories [the minus sign both in the second and third lines of Scheme 1].

4. Newton's constant. In some (very special) cases [2], the action for the effective gravitational field in quantum liquids is similar to the Einstein action

$$S_{\text{Einstein}} = -\int d^4x \frac{\sqrt{-g}}{16\pi G}\mathcal{R}. \qquad (2)$$

As in the case of Sakharov's induced gravity [6], the analog of the gravitational constant G in quantum liquids is determined by Planck's energy cutoff E_{Planck} (played by the amplitude of the superfluid gap Δ_0) and by the number of the chiral fermionic species: $G^{-1} \sim N_F E_{\text{Planck}}^2/\hbar$. Since G is determined by microscopic physics, it is not fundamental on the microscopic level (minus sign in the third line).

In quantum liquids, the effective G depends on temperature [2], $G^{-1}(T) = G^{-1}(0) + \gamma N_F T^2/\hbar$, where γ is the dimensionless factor of the order of unity. Since the temperature correction does not contain microscopic parameters and thus, in principle, can be obtained within the effective theory, G is not fundamental even on the effective level. But its vacuum value $G(T = 0)$ is fundamental for an inner observer.

Moreover, the phenomenological parameter $G(T = 0)$ of the effective theory, as viewed by the external observer, has a definite value for the quantum liquid isolated from the environment. That is why it can be considered as a fundamental constant in the effective theory, whence the plus sign in the second line of the G column.

5. Fine-structure constant. In logarithmic approximation, the action for effective electrodynamics

emerging in ^{3}He-A (and in other systems of the Fermi-point universality class) is [2]

$$S_{\rm em} = \frac{1}{\hbar}\int dt d^3x \frac{\sqrt{-g}}{16\pi\alpha} F^{\mu\nu}F_{\mu\nu}. \quad (3)$$

An analog of the fine-structure constant α is not fundamental both on the microscopic and effective levels, since it logarithmically depends both on the ultraviolet and infrared cutoff parameters. If the largest infrared cutoff is supplied by temperature, one has $\alpha^{-1} \sim N_F \ln(E_{\rm Planck}/T)$, where N_F is again the number of chiral fermionic species, and the ultraviolet cutoff is determined by the same Planck's scale $E_{\rm Planck} = \Delta_0$, which enters the effective Newton's constant [2]. It is the same effective electrodynamics as was discussed by Zel'dovich [7]. The dependence on $E_{\rm Planck}$ shows that α is not fundamental on the microscopic level; the dependence on the low-energy scale demonstrates that it is so not fundamental within the effective theory. In contrast to the Newton's constant, in the limit $T = 0$ and zero mass of all Standard Model fermions, the constant α vanishes. That is why the α column contains only the minus signs in Scheme 1.

Equation (3) does not contain speeds of light c_x, c_y, and c_z explicitly: these functions are hidden in the metric field. The anisotropic speed of light is the crucial argument that the decomposition of the dimensionless running coupling α into dimensionful e^2, $\hbar$, and c is meaningless: e^2 and c do not enter explicitly any covariant and gauge-invariant equations. For example, the energy levels of the electron in the hydrogen atom is determined by α and the rest energy M_e of an electron [8]:

$$E_{n,j} = M_e\left[1 - \frac{\alpha^2}{2n^2} - \frac{\alpha^4}{2n^4}\left(\frac{n}{j+1/2} - \frac{3}{4}\right) + \ldots\right]. \quad (4)$$

Recall that, in contrast to the quantity e, the physical electric (or other) charge of elementary particles in the Standard Model and its analog in ^{3}He-A are dimensionless (integer or fractional) quantities determined by geometry. They are determined either by gauge groups in fundamental gauge theories or by momentum-space topology in quantum vacua of the Fermi-point universality class.

The only fundamental constant which enters explicitly the electromagnetic action is $\hbar$.

6. What constants are really fundamental? Thus, in our example of the relativistic quantum field theory arising in quantum liquids, the only fundamental constant is $\hbar$. Since it is fundamental, it is possible to use it as a conversion factor of energy to frequency, as is stated by Duff *et al.* in [9] (of course, with the following reservations: (i) energy is additive while frequency is not; (ii) as distinct from frequency, the magnitude of energy depends on the choice of zero energy level; (iii) the frequency can be bounded from above due to, say, discreteness of time, while the energy is not bounded: it can be the sum of energies of many low-energy particles; etc.).

However, it is not completely excluded that $\hbar$ can arise as a result of a more fundamental theory above the Planck's scale which gives rise to the quantum mechanics in the low-energy scale [5].

In such a $\hbar$ case, the only fundamental constants which remain in the effective RQFT are the dimensionless charges and dimensionless topological quantum numbers [10, 2], which enter the topological terms in effective action. Such terms are naturally dimensionless, since they are determined either by the gauge groups or the topological invariants in real and momentum spaces. In 3+1 systems, such invariants describe the chiral anomaly [11, 12] and other anomalies. In 2+1 systems, these topological quantum numbers lead to the quantization of physical parameters such as Hall and spin Hall conductivities, which, being written in covariant form, are integer of rational numbers.

REFERENCES

1. J.-P. Uzan, Rev. Mod. Phys. (in press); hep-ph/0205340.
2. G. E. Volovik, Phys. Rep. **351**, 195 (2001); G. Volovik, *Universe in a Helium Droplet* (Oxford Univ. Press, Oxford, 2003) (in press), http://ice.hut.fi/Volovik/book.pdf.
3. R. B. Laughlin and D. Pines, Proc. Natl. Acad. Sci. USA **97**, 28 (2000).
4. S. Weinberg, in *The Constants of Physics*, Ed. by W. H. McCrea and M. J. Rees; Philos. Trans. R. Soc. London, Ser. A **310**, 249 (1983).
5. S. Adler, hep-th/0206120.
6. A. D. Sakharov, Dokl. Akad. Nauk SSSR **177**, 70 (1967) [Sov. Phys. Dokl. **12**, 1040 (1968)].
7. Ya. B. Zel'dovich, Pis'ma Zh. Éksp. Teor. Fiz. **6**, 922 (1967) [JETP Lett. **6**, 345 (1967)].
8. S. Weinberg, *The Quantum Theory of Fields* (Cambridge Univ. Press, Cambridge, 1995).
9. M. J. Duff, L. B. Okun, and G. Veneziano, JHEP **03023**, 1 (2002); physics/0110060.
10. D. J. Thouless, *Topological Quantum Numbers in Nonrelativistic Physics* (World Scientific, Singapore, 1998).
11. S. Adler, Phys. Rev. **177**, 2426 (1969).
12. J. S. Bell and R. Jackiw, Nuovo Cimento A **60**, 47 (1969).

JETP Letters, Vol. 76, No. 2, 2002, pp. 80–83. From Pis'ma v Zhurnal Éksperimental'noĭ i Teoreticheskoĭ Fiziki, Vol. 76, No. 2, 2002, pp. 92–94.

T-Odd Correlation in Polarized Neutron Decay¶

V. V. Bytev and E. A. Kuraev*

Joint Institute for Nuclear Research, Dubna, Moscow region, 141980 Russia

**e-mail: kuraev@thsun1.jinr.ru*

Received June 10, 2002

Abstract—*T*-odd correlation $[\mathbf{p}_e, \mathbf{p}_\nu]\boldsymbol{\eta}$ appears in the lowest order radiative correction to the polarized-neutron decay width, where $\boldsymbol{\eta}$ is the polarization vector of a neutron. It appears as a consequence of the final-state interaction and should not be confused with real CP violation of the Standard Model. The asymmetry has the order of 10^{-5}. Final-state interaction in the decay of an unpolarized neutron causes the appearance of transverse polarization of a recoil proton and electron. Explicit expressions are given. © *2002 MAIK "Nauka/Interperiodica"*.

PACS numbers: 13.30.-a; 13.88.+e; 13.40.Ks

Nowadays, interest in neutron β decay is twofold. It provides an independent way to extract Cabbibo–Kobayashi–Maskawa (CKM) matrix element V_{ud} and is the laboratory for the most precise measurement of CP(*T*)-violating effects. The role of radiative corrections (RC) to the theoretically calculated width becomes essential. Works devoted to the calculation of RC from the late 1960s up to now [1] concern mainly neutron lifetime and the behavior of the electron spectrum. RC as a source of CP-violating effects, which is the subject of this work, was first considered in 1967 by Callan and Treiman [2] for the case of nuclear β decay. Keeping in mind experimental interest in the *T*-odd correlation in the hope of discovering new physics, more information on the decay rate distribution is needed. This is the motivation for this work, in which we consider the effect of the nonzero imaginary part of one-loop RC to the matrix element. In section 1, we consider the first consequence of this RC to the CP(*T*)-odd correlation in the differential decay rate.

In section 2, we present the degree of electron and proton polarization for the case of unpolarized neutron decay, which is due to the imaginary part of RC to the matrix element.

In the discussion, we dispute the approach used in an experimental search for the *T*-odd effects.

The appendix is devoted to the details of calculation.

1. CP(*T*)-odd correlation. CP(*T*)-violating correlation for neutron β decay is on the order of 10^{-5} and can provide an essential background compared to tiny effects $\approx 10^{-8}$ associated with the phases of the CKM matrix. The CP(*T*)-odd correlation due to the final-state interaction is connected with the quantity $[\mathbf{p}_e, \mathbf{p}_\nu]\boldsymbol{\eta}$ in the differential decay rate ($\mathbf{p}_e$ and $\mathbf{p}_\nu$ are the 3-momenta of electron and neutrino in the neutron rest frame; $\boldsymbol{\eta}$ is the neutron polarization vector) and is defined as

$$\frac{\Gamma_{\text{odd}}}{\Gamma_0} = \frac{\text{Im}\sum M_0 M^{(1)*}}{\sum |M_0|^2} = |\boldsymbol{\eta}_z| NF(\theta, E), \qquad (1)$$
$$N = \alpha m/4M \approx 10^{-6}.$$

Here, the summation is over the electron and proton spin states, and $|\eta_z|$ is the projection of neutron polarization vector onto the transversal to the production plane formed by the electron and proton momentum vectors. M_0 is the matrix element of neutron β decay:

$$n(p_n, \boldsymbol{\eta}) \qquad p(p_p) + e(p_e) + \nu(p_\nu),$$
$$M_n = M = E + E_\nu + E_P, \quad \mathbf{p}_p + \mathbf{p}_e + \mathbf{p}_\nu = 0,$$
$$M_0 = \frac{G}{\sqrt{2}} V_{ud} \bar{u}_p \gamma_\alpha (1 + \lambda\gamma_5) u_n \bar{u}_e \gamma_\alpha (1 + \gamma_5) u_\nu, \qquad (2)$$
$$\lambda = a e^{-i\phi}, \quad a = g_A/g_V,$$

and $d\Gamma_0$ is the differential decay rate [3]:

$$d\Gamma_0 = \frac{G^2}{4\pi^3} |V_{ud}|^2 \sqrt{(E^2 - m^2)} (\Delta - E)^2$$
$$\times E\rho(1 + 3a^2)\left(1 + \mathbb{O}\left(\frac{m}{M}\right)\right) dE dc, \qquad (3)$$
$$\rho = 1 + \mathcal{A}\frac{\mathbf{p}_e \mathbf{p}_\nu}{E E_\nu} + \boldsymbol{\eta}\left[A\frac{\mathbf{p}_e}{E} + B\frac{\mathbf{p}_\nu}{E_\nu} + D\frac{\mathbf{p}_e \times \mathbf{p}_\nu}{E E_\nu}\right],$$
$$\Delta = M - Mp = 1.29 \text{ MeV}.$$

Here, $E_\nu = \Delta - E$ is the neutrino energy, E is the electron energy, and $\Gamma c = \cos\theta\Gamma\theta$ is the angle between the electron and neutrino 3-momenta. The explicit form of quantities $\mathcal{A}$, A, B, C, and D will be given below. Furthermore, we put here $E_P = M_p$ and neglect the contri-

¶This article was submitted by the authors in English.

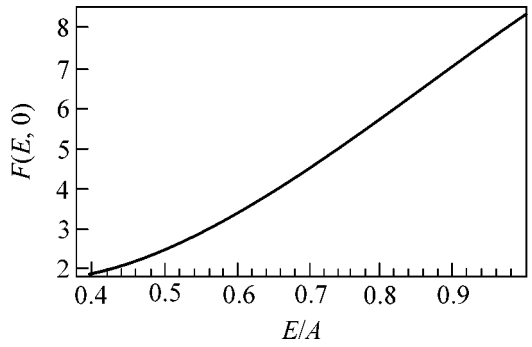

Fig. 1. Dependence of $F(E, \theta)$ on E for $\theta = 0$ and $\eta_z = |\boldsymbol{\eta}|$.

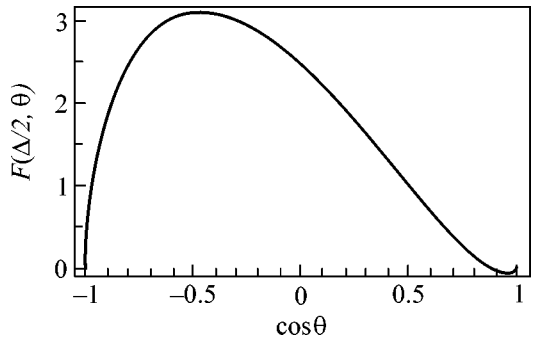

Fig. 2. Dependence of $F(E, \theta)$ on $c = \cos\theta$ for $E = \Delta/2$ and $\eta_z = |\boldsymbol{\eta}|$.

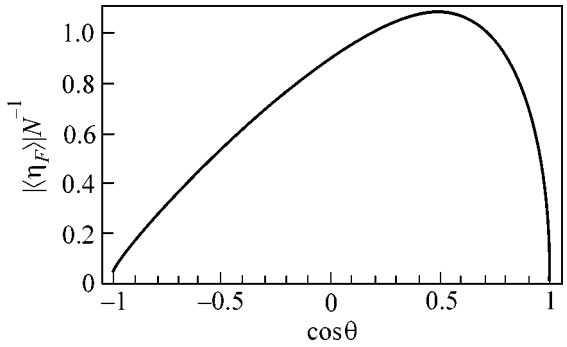

Fig. 3. Dependence of electron polarization on $c = \cos\theta$ for $E = \Delta/2$.

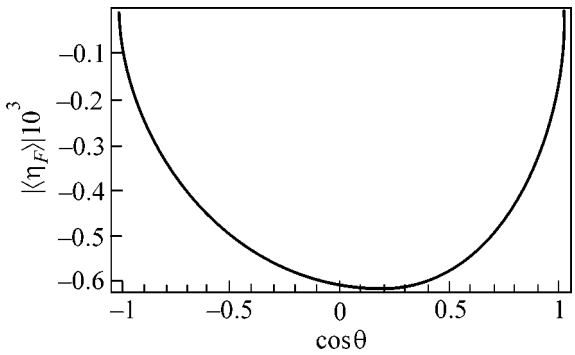

Fig. 4. Dependence of proton polarization on $c = \cos\theta$ for $E = \Delta/2$.

bution of the quantities on the order of electron-to-neutron mass ratio $m/M \ll 1$.

Among the set of Feynman diagrams describing one-loop RC, only one is relevant (it has nonzero imaginary part), which corresponds to the virtual photon exchange between an electron and a proton (final-state interaction):

$$M^{(1)} = \frac{GV_{ud}}{\sqrt{2}}\frac{\alpha}{4\pi} \times \int \frac{d^4k}{i\pi^2}\frac{\bar{u}_p\gamma_\mu(p+k+M_p)\gamma_\alpha(1+\lambda\gamma_5)u_n}{(k^2-\lambda^2)((p_p-k)^2-M_p)} \times \frac{\bar{u}_e\gamma_\mu(p_e-k+m_e)\gamma_\alpha(1+\gamma_5)u_\nu}{((p_e-k)^2-m_e^2)}. \quad (4)$$

Using the formulas given in the Appendix, we obtain for the *T*-odd correlation function [which was defined in Eq. (1)]

$$F(\theta, E) = \frac{E}{\rho m}\left[(a^2-1)\left[3\left(\frac{E_\nu}{E}\right)^2 - 4 - 6v\frac{E_\nu}{E}\cos\theta\right] + v^2(a-1)(13a+9)\right]\sin\theta, \quad (5)$$

where $v = \sqrt{1-(m/E)^2}$ is the electron velocity. This function is tabulated in Figs. 1 and 2.

2. Polarization degree of final particles. Another consequence of the nonzero imaginary part of $M^{(1)}$ consists in the appearance of electron and proton polarizations for the case of unpolarized neutron decay, which has the following form:

$$\langle\eta_p\rangle = N\frac{E\sin\theta}{m\rho(1+3a^2)}\mathbf{n}\left[(a^2-1) \times \left[3\left(\frac{E_\nu}{E}\right)^2 + 9v^2 + 6v\frac{E_\nu}{E}\cos\theta\right] + 4(a-1)^2\right], \quad (6)$$

$$\langle\eta_e\rangle = \frac{\alpha\sin\theta(1-a^2)m}{\rho E(1+3a^2)}\mathbf{n},$$

where unit vector $\mathbf{n}$ is directed along the vector $[\mathbf{p}_e \times \mathbf{p}_\nu]$. The magnitude of induced proton spin $\langle\eta_p\rangle$ is small enough ($\approx 10^{-5}$), whereas $\langle\eta_e\rangle$ is on the order of the anomalous magnetic moment of an electron (see Figs. 3, 4).

We note that both the *T*-odd correlation and the induced final electron and proton polarizations turn to zero at $a = 1$.

3. Discussion. Coefficients $\mathcal{A}$, *A*, *B*, *C*, and *D* entering into the Born differential decay rate (1)

$$\mathcal{A} = \frac{1-a^2}{1+3a^2}, \quad A = -2\frac{a^2+a\cos\phi}{1+3a^2},$$
$$B = 2\frac{a^2-a\cos\phi}{1+3a^2}, \quad D = 2\frac{a\sin\phi}{1+3a^2} \tag{7}$$

are connected with the magnitude and phase of the ratio of axial vector to the vector form factors of the nuclei. The results of recent experiments (see [4, 5]) are

$$a = |\lambda| = 1.2670 \pm 0.0035,$$
$$\phi = 180.07 \pm 0.18, \tag{8}$$

and the coefficient *D* [6]

$$D = (-0.6 \pm 1.2 \pm 0.5) \times 10^{-3} \tag{9}$$

is consistent with zero at the modern level of accuracy. The coefficient *D* is sensitive to the possible scalar- and tensor-type forces in weak interaction [7], whose contribution is also on the level of 3×10^{-5}. Further information can be found in [6].

Our hope is that on the next level of experimental accuracy our formulas will be relevant.

Our main result is Eq. (5) for the differential decay rate as a function of energy and emitting angle of an electron, which is illustrated in Figs. 1 and 2 as the distribution in the emission angle at the typical electron energy ($E \approx \Delta/2$) and the distribution in electron energy at a fixed emission angle.

Another result is given by the formulas for the induced average proton- and electron-spin polarization vectors directed normally to the production plane [see Eq. (6)].

We are grateful to A. Ali and G. Bunatyan for discussions. We are also grateful to V.N. Samoilov (NCPIDINR) and to the Heisenberg–Landau fund for support.

APPENDIX

For the one-spin correlation, the imaginary parts of the vector and tensor one-loop Feynman integrals are required:

$$I_\mu;\ I_{\mu\nu} = \int \frac{d^4k}{i\pi^2} \frac{k_\mu;\ k_\mu k_\nu}{k^2((p_e-k)^2 - m_e^2 + i0)} \times \frac{1}{((k+p_p)^2 - M_p^2 + i0)}. \tag{10}$$

Using the Feynman denominator-joining procedure, we introduce two Feynman parameters:

$$x((k-p_e)^2 - m_e^2 + i0) + (1-x)((k+p_p)^2 - M_p^2 + i0) = k^2 - 2kp_x + i0,$$
$$y(k^2 - 2kp_x) + (1-y)k^2 = (k - yp_x)^2 - y^2p_x^2 + i0,$$
$$p_x = xp_e - (1-x)p_p. \tag{11}$$

The imaginary part arises from the region where $p_x^2 < 0$. We take it in the form

$$p_x^2 = m_e^2 x + M_p^2(1-x) - sx(1-x) = s(x-x_-)(x_+-x),$$
$$x_\pm = \frac{M_p^2 + p_ep_p \pm R}{s}, \tag{12}$$
$$R = \sqrt{(p_ep_p)^2 - M_p^2m_e^2}, \quad s = (p_e+p_p)^2.$$

We use further

$$\mathrm{Im}\int_0^1 \frac{f(x)dx}{p_x^2 - i0} = \frac{\pi}{2R}[f(x_-) + f(x_+)]. \tag{13}$$

Using these formulas and standard algebraical technique, we calculate

$$\mathrm{Im}[I_\mu] = A_ep_{e\mu} + B_pp_\mu;$$
$$\mathrm{Im}[I_{\mu\nu}] = Eg_{\mu\nu} + Fp_{e\mu}p_{e\nu} + Gp_{p\mu}p_{p\nu} + H(p_{p\mu}p_{e\nu} + p_{p\nu}p_{e\mu}), \tag{14}$$

with

$$A_e = -\frac{\pi}{2R}(x_+ + x_-); \quad B_p = \frac{\pi}{2R}(2 - x_+ - x_-),$$
$$E = \frac{1}{4}\frac{\pi}{2R}[(m^2 - M^2)(x_+ + x_-) - s(x_+ + x_- - 2(x_-^2 + x_+^2))],$$
$$F = -\frac{1}{2}\frac{\pi}{2R}[x_-^2 + x_+^2], \quad G = -\frac{1}{2}\frac{\pi}{2R}[\bar{x}_-^2 + \bar{x}_+^2],$$
$$H = \frac{1}{2}\frac{\pi}{2R}[x_-\bar{x}_- + x_+\bar{x}_+], \quad \bar{x} = 1 - x. \tag{15}$$

REFERENCES

1. F. Gluck and K. Toth, Phys. Rev. D **46**, 2090 (1992); Y. Yokko, S. Suzuki, and M. Morita, Prog. Theor. Phys. **50**, 1894 (1973).

2. C. G. Callan and S. B. Treiman, Phys. Rev. **162**, 1494 (1967); J. D. Jackson, S. B. Treiman, and H. W. Wyld, Jr., Nucl. Phys. **4**, 206 (1957).
3. L. B. Okun, *Leptons and Quarks* (Nauka, Moscow, 1990; North-Holland, Amsterdam, 1984); S. M. Bilenky, R. M. Ryndin, Ya. A. Smorodinsky, and Ho Tso-shiu, Zh. Éksp. Teor. Fiz. **37**, 1758 (1959) [Sov. Phys. JETP **10**, 1241 (1960)].
4. C. Caso *et al.*, Eur. Phys. J. C **3**, 1 (1998) and (1999) off-year partial update for 2000 edition available on the PDC WWW pages (URL: http://pgb.lbl.gov/).
5. B. G. Erosolimski, Usp. Fiz. Nauk **116**, 145 (1975) [Sov. Phys. Usp. **17**, 377 (1975)]; B. G. Erosolimski *et al.*, Pis'ma Zh. Éksp. Teor. Fiz. **20**, 745 (1974) [JETP Lett. **20**, 345 (1974)].
6. L. Lising *et al.*, nucl-ex/0006001 (2000); T. Soldner *et al.*, in *Neutron Spectroscopy, Nuclear Structure, Related Topics: IX International Seminar on Interaction of Neutrons with Nuclei (ISINN-9), Dubna, 2001*, p. 49.
7. C. G. Carnoy, J. Deutsch, and P. Quinn, Nucl. Phys. A **568**, 256 (1994).

JETP Letters, Vol. 76, No. 2, 2002, pp. 84–87. Translated from Pis'ma v Zhurnal Éksperimental'noĭ i Teoreticheskoĭ Fiziki, Vol. 76, No. 2, 2002, pp. 95–98.

Three-Dimensional Spiral Structures in a Ferromagnet

A. B. Borisov

Institute of Metal Physics, Ural Division, Russian Academy of Sciences,
ul. S. Kovalevskoĭ 18, Yekaterinburg, 620219 Russia
e-mail: Borisov@imp.uran.ru

Received April 16, 2002; in final form, June 13, 2002

Abstract—New types of three-dimensional spiral structures are found in an isotropic ferromagnet. © *2002 MAIK "Nauka/Interperiodica".*

PACS numbers: 75.60.Ch; 75.50.-y; 61.72.Ji

Three-dimensional point defects—hedgehogs (Bloch points)—have been observed experimentally and studied in detail theoretically for nematic liquid crystals [1, 2] and ferromagnets, where these defects separate two portions of Bloch line with different magnetic polarities or different senses of magnetization rotation [3]. In the materials with cylindrical magnetic domains (CMDs), Bloch points are formed through thermal activation or by an external magnetic field in the region on the Bloch line where the applied field compensates the stray field. The hedgehog nucleation leads to the annihilation of Bloch lines, which are necessary for stabilizing the CMDs in high bias fields. The presence (influence) of Bloch points is most significant in the regions on the order of magnetic length, where the exchange energy far exceeds the anisotropy and magnetostatic energies and the distribution of unit vector $\mathbf{m}$ of the magnetization $\mathbf{M} = \mathbf{m}M_0$ obeys the Landau–Lifshitz equation in the exchange approximation:

$$[\mathbf{m}, \Delta\mathbf{m}] = 0, \quad \mathbf{m}^2 = 1. \tag{1}$$

The same equations determine the distribution of the director field in nematic liquid crystals (in the one-parameter approximation), and they are equivalent to the n-field equations ($D = 3$ and $N = 3$). The hedgehog-type configurations correspond (except for rotations and reflections) to the partial solution

$$\mathbf{m} = \mathbf{r}/r, \quad \mathbf{r} = \{x, y, z\}, \quad r = \sqrt{x^2 + y^2 + z^2} \tag{2}$$

of these equations. The topological classification of hedgehogs is based on mapping a closed surface σ (with coordinates θ and ϕ) enveloping the hedgehog center onto the degeneracy space S^2 [1], and the hedgehog topological charge (degree of mapping)

$$N = \frac{1}{4\pi}\int\int(\mathbf{m}[\mathbf{m}_\theta, \mathbf{m}_\phi])d\theta d\phi, \tag{3}$$

is unity.

In this work, a new procedure is suggested for integrating Eqs. (1), and a broad class of exact analytic solutions is found. On this basis, new types of three-dimensional structures are predicted for a ferromagnet: spiral and cnoidal hedgehogs.

In the angular variables Θ and Φ parametrizing vector $m = \{\sin\Theta\cos\Phi, \sin\Theta\sin\Phi, \cos\Theta\}$, Eqs. (1) are rewritten as

$$\Delta\Theta = \frac{\sin 2\Theta}{2}(\nabla\Phi)^2, \quad \nabla(\sin\Theta^2\nabla\Phi) = 0. \tag{4}$$

Following the procedure suggested in [4], we assume that the field $\Theta(\mathbf{r})$ depends locally $\Theta(a(\mathbf{r}))$ on an auxiliary field $a(\mathbf{r})$. Then one can readily make sure by direct mathematics that Eqs. (4) follow from the equations

$$\Theta''(a) = \sin 2\Theta(a)/2, \tag{5}$$

$$\Delta a = 0, \quad \Delta\Phi = 0, \quad (\nabla a)^2 = (\nabla\Phi)^2, \quad (\nabla a, \nabla\Phi) = 0 \tag{6}$$

for the fields $\Theta(a)$, $a(\mathbf{r})$, and $\Phi(\mathbf{r})$. It will be seen below that one can obtain a broad class of solutions to nonintegrable Eq. (1) with this anzatz, but it does not provide the full set of solutions. The vector fields (∇a) and $(\nabla\Phi)$ are normals to the surfaces $a = \text{const}$ and $b = \text{const}$, and, from the geometrical point of view, the solution to the system of Eqs. (6) determines two orthogonal harmonic ($\Delta a = 0$, $\Delta\Phi = 0$) coordinate surfaces with equal normal lengths.

Let us introduce complex variables $X = x + iy$ and $Y = x - iy$ and write the system of Eqs. (6) in the form of two equations

$$4\Omega_{,XY} = \Omega_{,zz}, \quad 4\Omega_{,X}\Omega_{,Y} = \Omega_{,z}^2 \tag{7}$$

for the complex function $\Omega = a + i\Phi$. By eliminating $\Omega_{,z}$ from the second equation and substituting this expres-

sion into the first equation, one arrives at the second-order equation

$$\Omega_{,XX}\Omega_{,Y}^2 + \Omega_{,YY}\Omega_{,X}^2 - 2\Omega_{,XY}\Omega_{,Y}\Omega_{,X} = 0. \quad (8)$$

After the substitution $\Omega_{,Y} = \Gamma\Omega_{,X}$, this general covariant [with respect to the transformations $\Omega \longrightarrow f(\Omega)$ for an arbitrary function f] equation reduces to the hydrodynamic equation of the Hopf type in complex variables. As a result, Eq. (7) is reduced to the system of equations

$$\Omega_{,Y} = \Gamma\Omega_{,X}, \quad \Omega_{,z} = 2i\sqrt{\Gamma}\Omega_{,X}, \quad (9)$$

where the field Γ satisfies the closed system of equations

$$\Gamma_{,Y} = \Gamma\Gamma_{,X}, \quad \Gamma_{,z} = 2i\sqrt{\Gamma}\Gamma_{,X}. \quad (10)$$

The last equation in Eqs. (10) is the condition for compatibility of Eqs. (9). One can show using scaling transformations that, for a constant field Γ, the solution to Eqs. (9) depends only on two spatial variables. For $\Gamma \neq$ const, it immediately follows from Eqs. (9) and (10) that the field Ω is an analytic function of field Γ,

$$\Omega = F(\Gamma), \quad (11)$$

and that the field $\Gamma(X, Y, z)$ is determined from the solution to the implicit equation

$$G(\Gamma, X + Y\Gamma + 2i\sqrt{\Gamma}z) = 0 \quad (12)$$

with an arbitrary function G. Note that the point (Θ = const, Φ = const) is imaged on the magnetization vector sphere by a constant complex number Γ and, hence, by a straight line in the three-dimensional space. For this reason, the Hopf invariant, which is determined by the linking coefficient of the images of two points on the sphere, is zero for the obtained solutions.

As in the hydrodynamics of incompressible fluid, solutions (11) and (12) are, generally, ambiguous. We will analyze the manifold of solutions for the field $\Gamma(X, Y, z)$ determined from the equation $X + Y\Gamma + 2iz\sqrt{\Gamma} = 0$. In this case, Ω is the analytic function

$$\Omega = F(\omega), \quad \omega = \tan(\theta/2)\exp i\phi \quad (13)$$

[or antianalytic function $\Omega = F(\omega^*)$] of the complex variable of the ω-stereographic projection of a unit sphere in the three-dimensional space ($x = r\sin\theta\cos\phi$, $y = r\sin\theta\sin\phi$, $z = r\cos\theta$). Let us choose the solution to Eq. (5) in the form of a soliton lattice

$$\cos\Theta = \mathrm{sn}(a/k, k), \quad (0 < k < 1). \quad (14)$$

In the simplest (solitonic) case, one has $\Theta = 2\arctan[\exp a]$ for $k = 1$. Then the complex field $\Psi = \tan(\Theta/2)\exp i\Phi$ is equal to $\exp[\Omega]$, and Φ satisfies the duality equation $\Phi_{\omega^*} = 0$. For $\Omega = \ln\omega^N$, these solutions describe the hedgehogs with topological charge N. They were obtained in [5] from the corresponding duality equations.

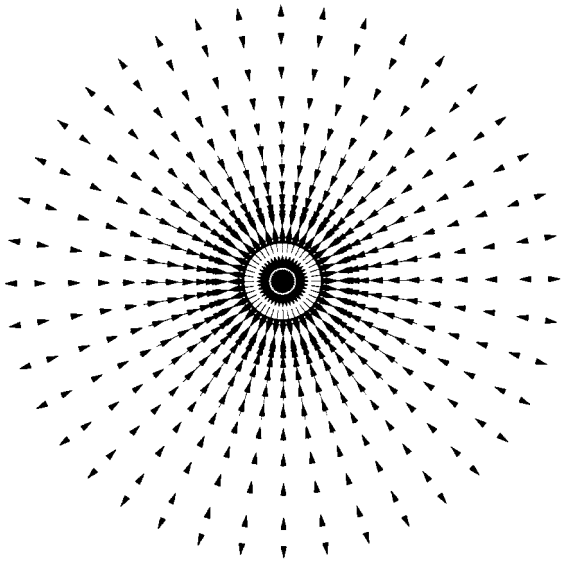

Fig. 1. Distribution of **m** for a cnoidal hedgehog with parameters $Q = 1$, $S = 0$, and $k = 1/3$ in the $z = 7$ plane.

In the case $k \neq 1$, we specify Ω by the vortex source potential $\Omega = a + i\Phi = (\alpha + i\beta)\ln\Omega$ ($\alpha, \beta \in R$). Then, the solution represents a linear defect with singular values of m_x and m_y along the axis $z(\theta \longrightarrow 0)$. It follows from the uniqueness requirement for magnetization that the field Φ must change by $2\pi Q$ ($Q \in Z$) upon going around the singularity line, while the change δa in field a $\delta a = 4kKS$ [$S \in Z$ and $K = K(k)$ is the complete elliptic integral of the first kind] is determined by the period $4K$ of elliptic function $\mathrm{sn}(u, k)$. As a result, the linear defect is characterized by the integral values S and Q, and the expressions for its magnetization z component and azimuthal angle have the form

$$\cos\Theta = \mathrm{sn}\left(\frac{Q\ln\tan(\theta/2)}{k} - \frac{2SK\phi}{\pi}\right), \quad (15)$$

$$\Phi = Q\phi + \frac{2kK\ln\tan(\theta/2)}{\pi}. \quad (16)$$

For the director field (except for its sign) in a nematic, the quantities Q and S can simultaneously take half-integer values.

The case $S = 0$ corresponds to the magnetic structure in the form of a cnoidal hedgehog consisting of an infinite set of domains. In the spherical layers $\theta \in (\theta_p, \theta_{p+1/2})$, $\phi \in [0, 2\pi]$ ($p \in Z$ and $\tan(\theta_p/2) = \exp[4pkK/Q]$), m_z is positive, and it is negative in the layers $\theta \in (\theta_{p-1/2}, \theta_p)$, $\phi \in [0, 2\pi]$. In the equatorial plane $z = 0$, the magnetization distribution coincides with a planar vortex. In the plane $z = h$ = const and in the vicinity of the singular line where $z \ll R = \sqrt{x^2 + y^2}$, the magnetization distribution corresponds to a set of ring domains representing a two- dimensional magnetic target [4] with $\cos\Theta = \mathrm{sn}(Q\ln(R/2h)/k, k)$ and the vorti-

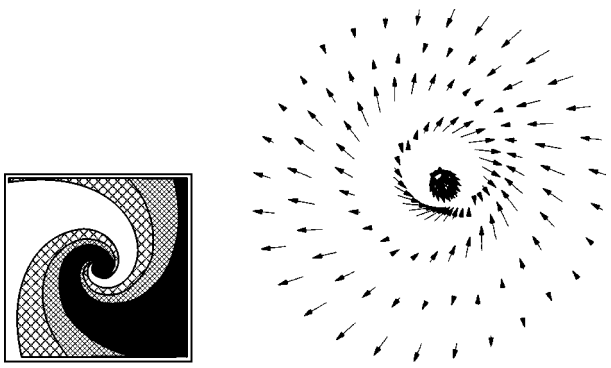

Fig. 2. Distribution of **m** for a spiral hedgehog with parameters $Q = 1$, $S = 1$, and $k = 1/3$ in the $z = 4$ plane. Inset: domains with (light region) $0 < \Theta < \pi/4$ and (dark region) $3\pi/4 < \Theta < \pi$ and the intermediate region $\pi/4 < \Theta < 3\pi/4$.

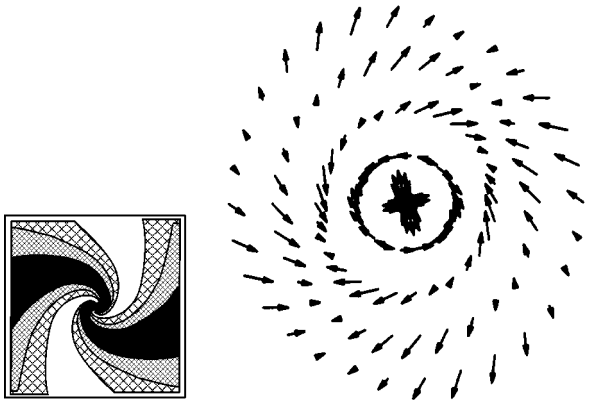

Fig. 3. Distribution of **m** for a spiral hedgehog with parameters $Q = 1$, $S = 2$, and $k = 1/3$ in the $z = 4$ plane.

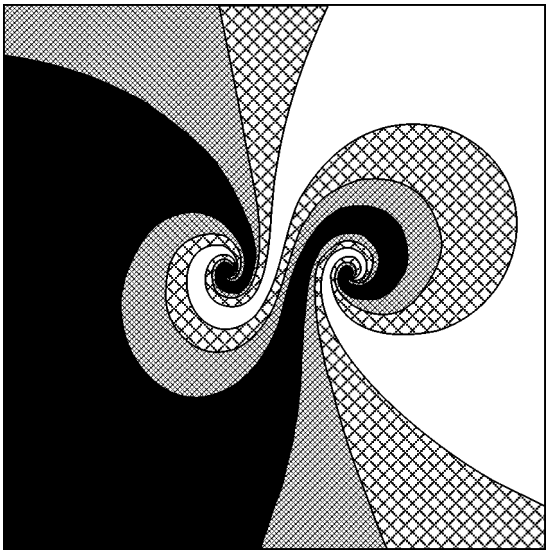

Fig. 4. The structure of a dipole composed of spiral hedgehogs with parameters $Q_1 = -Q_2 = 1$, $S = 2$, $S_1 = -S_2 = 1$, $k = 1/3$, $\theta_1 = \pi/2$, $\theta_2 = \pi/6$, and $\phi_1 = \phi_2 = 0$ in the $z = 2$ plane.

cal character of the m_x and m_y fields. The graph of **m** is given in Fig. 1. In the limiting case $k \longrightarrow 1$ and $\mathrm{sn}(u) \longrightarrow \tanh(u)$, the spherical layer $\theta \in (\theta_{-1/4}, \theta_{1/4})$, $\phi \in [0, 2\pi]$ near the equator covers the whole sphere, and the solution takes the simple form $\Theta = 2\arctan[(\tan(\theta/2))^Q]$, $\Phi = Q\phi$ with the topological charge Q. The energy $H = \int \nabla\mathbf{m}\nabla\mathbf{m}d^3x$ of a cnoidal vortex diverges at $\theta \longrightarrow 0$, and the integral (as in the case of a vortex ring in a superfluid) should be cut off at the values $\theta \sim d/L\Gamma$ corresponding to atomic distances d. Within the logarithmic accuracy, $H = \pi[(1 - k^2)/k^2]Q^2L\ln(L/d)$, where L is the system size.

At $S \neq 0$, the magnetization z component takes a constant value $\cos\Theta = \mathrm{sn}(C)$ at the spiral surfaces $z = \pm R\sinh[2\phi KkS/\pi Q + Ck/Q]$ passing through the origin of coordinates. The values $C = 2Kp$ ($p \in Z$) separate in the spiral hedgehogs the region with opposite magnetization directions. The domain widths increase with increasing k. Near the singular line, where $z = h = \mathrm{const} \ll R$, the field m_z is equal approximately to $\mathrm{sn}\left(Q\ln\frac{R}{2h}/k - 2K\phi S/\pi, k\right)$ and represents the S-turn logarithmic spiral coinciding qualitatively with the spiral vortex in a two-dimensional ferromagnet [4]. The sense of spiral twisting is determined by the N/S sign. The graphs of **m** and m_z are given in Figs. 2 and 3 for $S = 1$ and $S = 2$ and finite z values.

The general unique solution to the system of interacting spiral hedgehogs

$$\Omega = a + i\Phi = \sum_{j=1}^{n}\left(\frac{2ikK}{\pi}S_j + Q_j\right) \times \ln\left(\tan\frac{\theta}{2}\exp(i\phi) - \tan\frac{\theta_j}{2}\exp(i\phi_j)\right) + w(\omega) \quad (17)$$

is characterized by an arbitrary meromorphic function $w(\omega)$, parameter k, integer-valued S_j and N_j, and arbitrary real constants θ_j and φ_j and contains a set of singular rays coming at angles θ_j and φ_j ($j = 1, \ldots, n$) from the origin of coordinates. In the z = const plane, it represents a set of S_j-turn spirals, as shown in Fig. 4 for $n = 2$.

The three-dimensional spiral structures described above can nucleate on the nonmagnetic linear defects. They can be observed in thin magnetic films possessing a large quality factor and a small uniaxial anisotropy constant. The latter changes the hedgehog configuration at large distances from the singular line.

I am grateful to E.A. Kuznetsov, A.P. Protogenov, and A.B. Shabat for fruitful discussions and useful remarks, to the participants of the session of the Nonlinear Dynamics Council at the Russian Academy of Sciences, and to S.A. Zykov for assistance in computer graphics. This work was supported in part by the Rus-

sian Foundation for Basic Research (project no. 00-01-00366) and by INTAS (grant no. 99-1782).

REFERENCES

1. G. E. Volovik and V. P. Mineev, Zh. Éksp. Teor. Fiz. **72**, 2256 (1977) [Sov. Phys. JETP **45**, 1186 (1977)].
2. M. V. Kurik and O. D. Lavrentovich, Usp. Fiz. Nauk **154**, 381 (1988) [Sov. Phys. Usp. **31**, 196 (1988)].
3. A. P. Malozemoff and J. C. Slonczewski, *Domain Walls in Materials with Cylindrical Magnetic Domains* (Academic, New York, 1979; Mir, Moscow, 1982).
4. A. B. Borisov, Pis'ma Zh. Éksp. Teor. Fiz. **73**, 279 (2001) [JETP Lett. **73**, 242 (2001)].
5. L. M. Pismen, *Vortices in Nonlinear Fields* (Clarendon, Oxford, 1999).

Translated by V. Sakun

JETP Letters, Vol. 76, No. 2, 2002, pp. 88–92. Translated from Pis'ma v Zhurnal Éksperimental'noĭ i Teoreticheskoĭ Fiziki, Vol. 76, No. 2, 2002, pp. 99–104.

Untwisting of the Helical Structure in a Plane Layer of Chiral Liquid Crystal

V. A. Belyakov

Landau Institute for Theoretical Physics, Russian Academy of Sciences, ul. Kosygina 2, Moscow, 117334 Russia

Received June 3, 2002

Abstract—The untwisting of the helical structure of a chiral liquid crystal (CLC) in a thin plane layer exposed to an external action (temperature or field) and its dependence on the molecular adhesive forces at the layer boundaries are studied theoretically. It is shown that the critical electric (magnetic) field for complete untwisting in a thin layer may be appreciably lower than in the corresponding bulk CLC sample, and, contrary to the latter, the untwisting proceeds jumpwise. The expressions relating the jump temperature (field), i.e., the magnitude of untwisting action, to the CLC material parameters, layer thickness, and surface adhesive potential are given. The jump temperature (field) hysteresis is studied. In particular, it is shown that, for certain parameters, the untwisted helix remains untwisted after the removal of external action. The revealed qualitative regularities of untwisting are illustrated by numerical computations with the use of particular parameters of a CLC layer. © *2002 MAIK "Nauka/Interperiodica"*.

PACS numbers: 61.30.Gd

1. It is known that an external electric (magnetic) field applied perpendicularly to the axis of the helical structure of a chiral liquid crystal (CLC) brings about distortion and untwisting of a helix (increase in pitch), and it becomes completely untwisted (the pitch becomes infinite) upon achieving a certain critical field [1, 2]. The phenomenon of helix distortion and untwisting in bulk CLC samples is well understood. In [1, 2], this effect was analyzed for cholesterics, and ferroelectric smectics were considered in [3]. In bulk cholesterics and smectics, the helix pitch increases smoothly with increasing applied field and becomes infinite in a critical field. Analogous helix untwisting was observed upon temperature-induced pitch variations in CLCs [4, 5].

The question of temperature- and field-induced helix untwisting in finite-thickness CLC layers has been inadequately studied. However, it is the finite-thickness (down to the molecular scale [6]) CLC layers which are now being intensively studied experimentally. They reveal some intriguing physical phenomena associated, in particular, with the adherence of CLC molecules at the layer boundaries. The effects occurring in the CLC layers and their influence on the optical properties are of a considerable practical interest, because it is the electrooptical properties of the CLC layers that underlie many important applications of CLCs in imaging and information processing systems.

It has long been established that, in the presence of surface adherence, the structure of CLC layers can undergo jumpwise changes, often of a hysteresis character [5, 9, 10], on the background of smooth field- [7, 8] or temperature-induced [4, 5] structural changes. For fields far enough from the critical value corresponding to the complete helix untwisting, the structural changes and their hysteresis in the CLC layers exposed to an external field were studied theoretically in [11], and the temperature-induced changes were considered in [12].

In this work, the structural changes and hysteresis are studied theoretically for the CLC layers exposed to near-critical external actions, and the dependence of the corresponding critical values (untwisting temperature and field) on the surface adhesive potential, layer thickness, and CLC material parameters are revealed. The analytic results are illustrated by numerical calculations.

2. The helical director distribution in a plane CLC layer is characterized, in particular, by the number N of helix half-turns across the layer thickness (we assume, for definiteness, that the alignment directions at both surfaces are identical). Immediately before the complete helix untwisting under an external action, the director configuration corresponds to $N = 1$, and $N = 0$ at the final untwisting stage. In the presence of surface adherence, N may somewhat differ from integer values, because the director orientations at the surfaces may depart from the alignment direction. Nevertheless, we will use integral numbers N nearest to the actual number of helix half-turns across the layer thickness (and which are exactly achieved upon smooth variation of the external action). The surface adhesive forces of LC molecules play an important role in the untwisting process [11, 12]. They give rise to pitch jumps and their hysteresis on the background of smooth pitch variations. By the field- or temperature-induced helix untwisting in a finite-thickness layer, we imply the jumpwise transition of director configuration from the

state with a single half-turn to the state with zero half-turns upon increasing field or varying temperature. It will be shown below that, depending on the surface adhesive forces, the helix untwisting in such a layer can occur in fields both lower than the critical untwisting field in a bulk sample and higher than this field.

The helix untwisting mechanism caused by the formation of defects in the director configuration will not be discussed in this work. By the untwisting mechanism and ensuing pitch jump will be meant the transition between the helix configurations differing by one half-turn as a result of overcoming the surface adhesive potential barrier by the director.

However, one should bear in mind that the actual jump field (helix untwisting field) depends on the zero-field helix configuration. Indeed, the helix-untwisting field depends on the zero-field angle φ (angle of director departure from the alignment direction at the surface). In the case that this angle is close to its critical value φ_c [12] corresponding to the pitch jump, the helix will undergo a jump into the configuration with zero half-turns upon applying even a weak field or at small temperature variations. If the angle φ is far from φ_c, the action magnitude required for the jump may be quite appreciable. The computational results for the critical field (jump temperature) in a CLC layer with finite surface adhesive forces are presented below.

3. Before discussing the field-induced helix untwisting in detail, let us consider the untwisting through a temperature-induced change in pitch. This process is more simple and pictorial, because the helix remains harmonic (undistorted) in this case, and only the helix pitch and the number N of half-turns across the layer thickness change with temperature. We consider an ideal plane CLC layer of a cholesteric liquid crystal for definiteness. We will also assume that the adhesive forces are identical at both layer surfaces, the initial layer state corresponds exactly to a single half-turn, i.e., to $N = 1$, and the director directions at both surfaces coincide with the alignment directions, the latter, in turn, being the same at both surfaces. In this situation, the helix pitch in the layer coincides with the pitch in an infinite cholesteric, and the temperature-induced changes in pitch are determined through the minimization of the layer free energy, which, following [4], can be written as

$$F(T) = 2W_s(\varphi) + (K_{22}d/2)(2\pi/p_d(T) - 2\pi/p(T))^2, \quad (1)$$

where K_{22} is the Frank's torsion modulus, $W_s(\varphi)$ is the surface adhesive potential, d is the layer thickness, $p(T)$ is the equilibrium helix pitch in a bulk cholesteric crystal at temperature T, $p_d(T)$ is the pitch in the layer at the same temperature, and φ was defined above. Because the pitch $p_d(T)$ in the layer is uniquely related to the angle φ and the equilibrium pitch $p(T)$ is uniquely related to the angle $\varphi_0(T)$ corresponding to the free director departure from the alignment direction in the absence of surface adherence, the expression for the free energy can be rewritten as a function of these angles, and a change in the angle φ upon changing pitch can be described by the following equation [12]:

$$\partial W_s(\varphi)/\partial\varphi + (2K_{22}/d)[\varphi - \varphi_0(T)] = 0. \quad (2)$$

The solution to Eq. (2) indicates [12] that, in the presence of surface adherence, the pitch in the layer may undergo, along with smooth variations, jumpwise changes with temperature. As was pointed out above, the pitch undergoes a jump upon achieving a certain critical value φ_c that is determined by the surface potential $W_s(\varphi)$. It follows from Eq. (2) that the free angle $\varphi_0(T)$ of director departure at the jump point (or the pitch in an infinite CLC) is related to the surface adhesive potential by the following expression:

$$\varphi_0(T_j) = \varphi_c + (\partial W_s(\varphi)/\partial\varphi)_\varphi = \varphi_c/(2WS_d), \quad (3)$$

where T_j is the jump temperature and $S_d = K_{22}/dW$ is the dimensionless parameter (W is the surface potential depth). Since the maximum possible change in angle φ_0 for the complete helix untwisting from the initial director configuration in a cholesteric layer with $N = 1$ is $\pi/2$, the complete untwisting (jump into the state with $N = 0$) can occur, according to this requirement and Eq. (3), not for all values of parameter S_d but only if it satisfies the inequality

$$S_d \geq [(\partial W_s(\varphi)/\partial\varphi)_\varphi = \varphi_c/2W]/(\pi/2 - \varphi_c). \quad (4)$$

For example, $\varphi_c = \pi/4$ for the model Rapini potential $W_s(\varphi) = -(W/2)\cos^2\varphi$ [4, 13, 14], and inequality (4) gives $S_d \geq 1/\pi$; i.e., the critical value of this parameter is $S_{dc} = 1/\pi$. This means that the untwisting cannot occur with varying temperature if the parameter S_d is smaller than its critical value. To illustrate quantitatively the temperature-induced variations of director configuration in a layer, we present the results for a model with the Rapini adhesive potential. The calculated temperature-induced changes in the director departure from the alignment directions at the layer surfaces (due to pitch variations) are shown in Fig. 1 for different values of parameter S_d. Typically, the pitch increases with lowering temperature. In this case, a decrease in temperature corresponds to a change in φ from zero to negative values in the right-hand bundle of curves. As the angle φ achieves its critical value φ_c, the helix undergoes jumpwise untwisting [indicated in Fig. 1 by the wavy arrows and corresponding to the jumps from the lower branches of the right-hand bundle of curves ($N = 1$) to the branches of the left-hand bundle ($N = 0$)], and φ can be determined from the left bundle corresponding to the configuration $N = 0$. One can see from the figure that, in accordance with condition (4), the transition from the state with a single half-turn to the state with no half-turns is not possible for all S_d values. For instance, the untwisting does not occur in a layer with $S_d = 1/2\pi$, although the helix is completely untwisted in an infinite

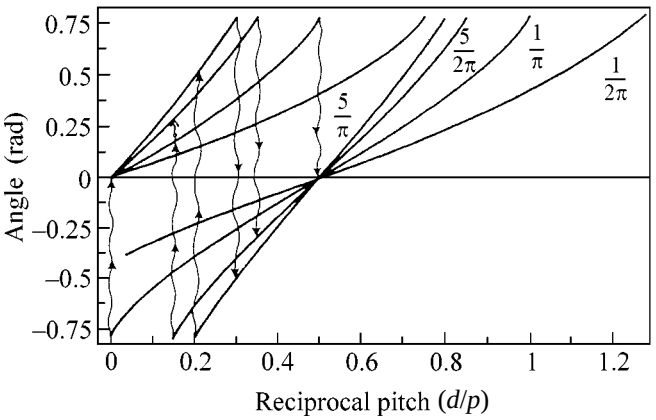

Fig. 1. Temperature dependences of the angle of director departure from alignment direction in the region of helix untwisting ($N = 0$ and 1) for different values of parameter S_d (indicated in the figure).

cholesteric at a certain temperature corresponding to $\varphi_0 = -\pi/2$ and $d/p = 0$. For the opposite jump in pitch, i.e., for its decrease with temperature (increase in φ in the upper curves at the left part of the figure), the jump exhibits temperature hysteresis; i.e., the pitch at which the helix configuration reverts jumpwise to the state with a single half-turn is different from the pitch corresponding to the forth transition. The smaller the value of S_d the larger the temperature hysteresis. The latter, according to Eqs. (2) and (3), is determined by the expressions

$$\begin{aligned} d(1/p(T_+) - 1/p(T_-)) &= (\partial W_s(\varphi)/\partial\varphi)_\varphi \\ &= \varphi_c/\pi W S_d + 1/2(4\varphi_c/\pi - 1), \\ d(1/p(T_+) - 1/p(T_-)) &= 1/2\pi S_d, \end{aligned} \tag{5}$$

where the second relationship corresponds to the Rapini potential, and T_+ and T_- are the jump temperatures, respectively, for the temperature increase and decrease. It should be noted that the director orientation in the layer is nonuniform and slightly changes from surface to surface after the jump into the state with $N = 0$ (which we called the helix untwisting state), although the resulting twist angle is much smaller than before the jump. For this reason, it would be more correct to refer to this process as helix pre-untwisting rather than helix untwisting. Note also that the director distribution can be made uniform throughout the whole layer by a slight change in the orientation of alignment directions at the layer surfaces. Because of this, the jump to the state with $N = 0$ will still be referred to below as "helix untwisting." A uniform director orientation after the jump can be obtained in a layer with changed alignment directions; namely, the latter must be turned at each surface through an angle φ_j (the angle after the jump in the problem with the same alignment directions at both surfaces) in the direction opposite to the helix rotation.

4. The problem of helix untwisting in an external field (electric or magnetic) is more complex because the applied field specifies a new anisotropy direction and the helix becomes distorted (nonharmonic) [1–3]. In addition, the CLC is, generally, deformed; the director departs from the plane perpendicular to the helix axis and the angle between the director and this axis varies [15]. To simplify the problem, it is reasonable to analyze some certain directions of the external field. Namely, we consider ideal plane CLC layers in an electric (magnetic) field perpendicular to the helix axis. We will consider the simplest situation for which only the field-induced torsional strain is taken into account. In this case, the angle between the director and the helix axis does not change, and the expression for the free energy volume density is [3, 15] (for cholesterics, $\mathbf{P}_s = 0$)

$$\begin{aligned} F_v(\mathbf{E}) &= (K_{22}/2)(d\varphi/dz - 2\pi/p_0)^2 \\ &+ EP_s\cos\varphi + (\varepsilon_a E^2/16\pi)\cos 2\varphi, \end{aligned} \tag{6}$$

where p_0 is the zero-field equilibrium helix pitch in a bulk CLC, φ is the azimuthal angle of molecular orientation measured from the field direction, ε_a is the dielectric anisotropy of CLC, and $\mathbf{P}_s$ is its spontaneous polarization. Therefore, the free energy in an external field is expressed by Eq. (1), in which the second term in the right-hand side should be replaced by $\int F_v(\mathbf{E})dv$, where the integration does over the layer volume.

It is also reasonable to consider the experimentally most natural field orientations perpendicular to the helix axis. We will restrict ourselves to the field directions along the alignment direction and perpendicular to it. Before discussing these two cases, let us reveal some untwisting features that are common to both these cases. For the moment, we ignore the dependence of untwisting on the field orientation about the alignment direction. This can be done if the field-induced helix distortion is ignored and only the increase in cholesteric helix pitch is taken into account. In this approximation, the field-induced helix untwisting is described by the equation analogous to the temperature case (2), in which the helix pitch of an infinite CLC, i.e., φ_0, should be taken as a function of applied field and not of the temperature.

Let us calculate the behavior of a CLC helix in an external field applied to a layer with Rapini surface adhesive potential. The results for the helix twisting angle as a function of the applied field (up to the level corresponding to the untwisting field in an infinite sample), i.e., for the angle of director rotation about the helix axis upon moving from one to the other layer surface, are given in Fig. 2 for different values of parameter S_d. The abscissa axis corresponds to the applied field E normalized to the untwisting field E_c in an infinite sample, and the ordinate axis is for one-half of the helix twist angle in the layer. For simplicity, the field depen-

dence of helix pitch in an infinite sample was taken in the analytic form given by Eq. (5) in [3]. The upper curves correspond to the twist angle for the initial state $N = 1$, and the lower curves describe the behavior after the jump into the director configuration with $N = 0$. In the approximation adopted, the field corresponding to helix untwisting in an infinite CLC does not induce untwisting in a layer with parameter S_d smaller than $1/\pi$, so that the field necessary for helix untwisting in the layer is higher than the untwisting field in an infinite sample.

For values larger than $1/\pi$, the untwisting (pitch jump) occurs in fields lower than the critical field in an infinite sample. Accordingly, the curve for $S_d = 1/2\pi$ in Fig. 2 shows no jump at $E \le E_c$, and, for $S_d > 1/\pi$, the jumps occur at $E \le E_c$. As in the case of temperature-induced untwisting, the magnitude of jump field hysteresis in the layer decreases with increasing S_d. For values of S_d smaller than $1/\pi$, the helix configuration does not revert to the initial $N = 1$ state in a decreasing field after the jump (which occurs at $E > E_c$) in the increasing field (this corresponds to the curves with $S_d = 1/2\pi$); i.e., the helix remains untwisted after removing the field and, hence, exhibits bistability in the applied field.

Let us discuss qualitatively how the picture of field-induced helix untwisting alters if one takes into account the dependence of helix distortion on the field direction. For simplicity, we consider a cholesteric, i.e., a CLC without spontaneous polarization. Physically, it is clear that, for the positive dielectric anisotropy and the field direction coinciding with the alignment directions, the director-orienting field effect will show up as a strengthening of the surface adhesive forces, and the helix-untwisting fields (jump fields) will be higher than in Fig. 2. For the field direction perpendicular to the alignment direction, the same field-orienting effect will show itself as a weakening of the surface adhesive forces, and the helix-untwisting fields (jump fields) will decrease compared to their values in Fig. 2.

After the jump, the parallel field aids the surface adhesive forces in creating uniform director orientation across the whole layer, so that the helix can be completely untwisted in a field lower than its critical value in an infinite sample. As for the field perpendicular to the alignment direction, it counteracts the surface adhesive forces in creating uniform director orientation across the layer after the jump, so that the uniform director orientation cannot be achieved in the field coinciding with its critical value in a bulk cholesteric. It is clear from the aforesaid that the field parallel to the alignment direction is favorable to the creation of a uniform director orientation in the layer. In this case, similarly to the temperature-induced helix untwisting, the uniform director orientation can be achieved in the layer immediately after the jump in a field lower than critical, provided that the alignment directions at the surfaces are slightly rotated.

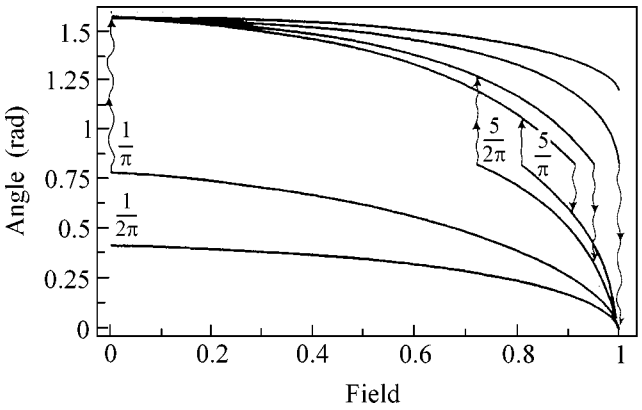

Fig. 2. Calculated field dependences of the helix twisting angle in the region of pitch jump ($N = 0$ and 1) for different values of parameter S_d (indicated in the figure).

5. Although the above picture of helix untwisting in the finite-thickness CLC layers is a model, it properly describes the qualitative aspect of the phenomenon. This is primarily true for jumpwise helix untwisting and its hysteresis that is caused by the surface adhesive forces and depends on the parameter S_d. Next, the magnitude of external action corresponding to the complete helix untwisting in a layer is different from its magnitude in an infinite CLC; in particular, it can be lower than in an infinite CLC. Of practical interest are the revealed bistability of director orientation in a layer exposed to an external field and the quantitative criterion for the bistability (restrictions on the parameter S_d), as well as the fact that the helix in the layer can be completely untwisted in the external field smaller than its critical value in an infinite CLC. As to the quantitative aspect, which is important for the description of the experimental results, it is reasonable to solve the equations numerically, e.g., using the approach suggested in [3, 12] for the parameters corresponding to a particular LC material and surface adhesive forces with regard to their dependence on the external action. It is also worth noting that the temperature fluctuations of director orientation, which were not taken into account in this work, can slightly change the quantitative results; the jump fields may be slightly shifted and the hysteresis magnitude may be reduced. The fluctuations in this system deserve separate consideration. However, the preliminary theoretical [11, 12] and experimental [5] results suggest that the role of fluctuations in thin layers is less important than in thick layers, and they do not change substantially the results obtained in this work.

REFERENCES

1. P. G. de Gennes, Solid State Commun. **6**, 123 (1968).
2. R. Dreher, Appl. Phys. Lett. **12**, 281 (1968).
3. V. A. Belyakov and V. E. Dmitrienko, Zh. Éksp. Teor. Fiz. **78**, 1568 (1980) [Sov. Phys. JETP **51**, 787 (1980)].

4. P. G. de Gennes and J. Prost, *The Physics of Liquid Crystals* (Clarendon, Oxford, 1993).
5. H. Zink and V. A. Belyakov, Mol. Cryst. Liq. Cryst. **265**, 445 (1995); G. Zink and V. A. Belyakov, Pis'ma Zh. Éksp. Teor. Fiz. **63**, 37 (1996) [JETP Lett. **63**, 43 (1996)].
6. P. O. Andreeva, V. K. Dolganov, R. Fouret, *et al.*, Phys. Rev. E **59**, 4143 (1999).
7. R. Dreher, Solid State Commun. **13**, 1571 (1973).
8. W. J. A. Goossens, J. Phys. (Paris) **43**, 1469 (1982).
9. W. Greubel, Appl. Phys. Lett. **25**, 5 (1974).
10. W. Kuczynski, private communication.
11. V. A. Belyakov and E. I. Kats, Zh. Éksp. Teor. Fiz. **120**, 430 (2001) [JETP **93**, 380 (2001)].
12. V. A. Belyakov and E. I. Kats, Zh. Éksp. Teor. Fiz. **118**, 560 (2000) [JETP **91**, 488 (2000)].
13. L. M. Blinov, E. I. Kats, and A. A. Sonin, Usp. Fiz. Nauk **152**, 449 (1987) [Sov. Phys. Usp. **30**, 604 (1987)].
14. L. M. Blinov and V. G. Chigrinov, *Electrooptics Effects in Liquid Crystal Materials* (Springer-Verlag, New York, 1994), Chap. 3.
15. S. A. Pikin, *Structural Transformations in Liquid Crystals* (Nauka, Moscow, 1981).

Translated by V. Sakun

JETP Letters, Vol. 76, No. 2, 2002, pp. 93–98. From Pis'ma v Zhurnal Éksperimental'noĭ i Teoreticheskoĭ Fiziki, Vol. 76, No. 2, 2002, pp. 105–109.

Microscopic Derivation of Ginzburg–Landau-Type Functionals for Alloys and Their Application to Studies of Antiphase and Interphase Boundaries¶

V. G. Vaks

Russian Research Center Kurchatov Institute, pl. Kurchatova 1, 123182 Moscow, Russia

e-mail: vaks@mbslab.kiae.ru

Received May 27, 2002; in final form, June 10, 2002

Abstract—The cluster methods described earlier are used to generalize the Ginzburg–Landau gradient expansion for the free energy of an inhomogeneous alloy to the case of not small values of order parameters and varied composition. The results obtained reveal a number of important differences from the expressions used in the phenomenological phase-field approach. Differential equations relating the local values of concentration and order parameters within the antiphase or interphase boundary (APB or IPB) are derived. These equations are applied to study the segregation at APBs near the phase-transition lines, the structure of APBs and IPBs near tricritical points, wetting APBs in phases with single and several order parameters, and also some effects of the anisotropy of APBs under $L1_0$- and $L1_2$-type orderings. © *2002 MAIK "Nauka/Interperiodica".*

PACS numbers: 81.30.Bx; 61.50.Ks; 05.70.Fh

Studies of inhomogeneous alloys attract interest from both fundamental and applied points of view, in particular, in connection with the microstructure evolution under phase transformations [1–12]. Typical inhomogeneities in such problems are antiphase or interphase boundaries (APBs or IPBs), which separate the differently ordered domains or the different phases. Both experimental and theoretical studies show that, in situations of practical interest, the APB or IPB width usually much exceeds the interatomic distance [5–12]. Therefore, Ginzburg–Landau (GL)-type gradient expansions can be used to describe the free energy of such states, even though the order parameters and concentration variations are typically not small, contrary to the assumptions of standard GL theory. Employing such generalized GL functionals (suggested first by Cahn and Hilliard [1]) is now referred to as the phase-field method, and it is widely used for different systems (see, e.g., [6–8]). However, a number of simplifying assumptions are usually employed in this phenomenological approach, and so its relation to more consistent theoretical treatments remains unclear. Recently, microscopic cluster methods have been developed for inhomogeneous alloys [9–13]. Below, I use these methods to derive the GL functionals and then apply them for studies of APBs and IPBs.

To be definite, I consider a binary alloy A_cB_{1-c} at $c \le 1/2$. Various distributions of atoms over lattice sites i are described by the mean occupations $c_i = \langle n_i \rangle$, where n_i is unity if the site i is occupied by atom A and zero otherwise, while averaging is taken, generally, over the space- and time-dependent distribution function [9]. The free energy $F\{c_i\}$ in the cluster description can be written as a series [13]

$$F = \sum_i f^i = \sum_i \left(F_1^i + \sum_j F_2^{ij} + \ldots + \sum_{j,\ldots,k} F_m^{ij\ldots k} \right). \quad (1)$$

Here, f^i is the free energy per site i; $F_1^i = T[c_i \ln c_i + (1 - c_i)\ln(1 - c_i)]$ is the mixing entropy contribution; $F_l^{i\ldots k} = F_l(c_i, \ldots, c_k)$ is the contribution of interactions within l-site cluster of sites $i, \ldots, k$; and m is the maximum cluster size considered. The simplest mean-field approximation (MFA) and the pair-cluster approximation (PCA) correspond to the neglect of many-site contributions $F_{m>2}$ in (1), while, in a more refined tetrahedron cluster approximation (TCA) (which should be used, in particular, to adequately describe the $L1_2$ and $L1_0$-type orderings [9]), Eq. (1) also includes 4-site terms F_4^{ijkl} [13].

For the homogeneous ordered structure, the mean occupation $c_j = c(\mathbf{r}_j)$ at site j with the lattice vector $\mathbf{r}_j$ can be written as the superposition of concentration waves with some superstructure vectors $\mathbf{k}_s$ [8–12]:

$$c_j = c + \sum_s \eta_s \exp(i\mathbf{k}_s\mathbf{r}_j) \equiv \sum_p \eta_p \exp(i\mathbf{k}_p\mathbf{r}_j). \quad (2)$$

Here, amplitudes η_s can be considered as order parameters; the last expression also includes the term with

¶This article was submitted by the author in English.

$\eta_p = c$ and $\mathbf{k}_p = 0$; and, for simplicity, both parameters η_s and factors $\exp(i\mathbf{k}_s\mathbf{r}_i)$ are supposed to be real, which is the case, in particular, for the B2 $L1_0$ and $L1_2$-type orders.

For weakly inhomogeneous states, amplitudes η_p in Eq. (2) are not constants but smooth functions of coordinates $\mathbf{r}_i$. Thus, functions $f^i\{c_j\}$ in (1) can be expanded in powers of differences $\delta c_j = \sum_p \delta\eta_p^j \exp(i\mathbf{k}_p\mathbf{r}_j)$, where

$$\delta\eta_p^j = \eta_p^j - \eta_p^i = \mathbf{r}_{ji}\nabla\eta_p + \frac{1}{2}r_{ji}^\alpha r_{ji}^\beta \nabla_{\alpha\beta}\eta_p. \qquad (3)$$

Here, $\eta_p = \partial\eta_p^i/\partial r_i^\alpha$, $\nabla_{\alpha\beta}\eta_p = \partial^2\eta_p^i/\partial r_i^\alpha \partial r_i^\beta$, $\mathbf{r}_{ji} = (\mathbf{r}_j - \mathbf{r}_i)$, and the summation over repeated Cartesian indices α, $\beta = 1, 2, 3$ is implied. After the substitution of these expressions into Eq. (1), one can proceed from the summation over i to the integration over continuous variable $\mathbf{r} = \mathbf{r}_i$. Making also standard manipulations with the part-by-part integration of terms with $\nabla_{\alpha\beta}\eta_p$ [2], one obtains for the GL functional

$$F = \frac{1}{v_a}\int d^3r\left[\sum_{p,q} g_{pq}^{\alpha\beta}\nabla_\alpha\eta_p\nabla_\beta\eta_q + f\{\eta_p\}\right]. \qquad (4)$$

Here, v_a is volume per atom; $f\{\eta_p\}$ is function $f^i\{c_j\}$ in Eq. (1) averaged over all sublattices with c_j given by Eq. (2); and $g_{pq}^{\alpha\beta}$ is given by the expression

$$g_{pq}^{\alpha\beta} = -\frac{1}{2}\sum_j r_{ij}^\alpha r_{ij}^\beta S_{ij}^i \exp[i(\mathbf{k}_p\mathbf{r}_j - \mathbf{k}_q\mathbf{r}_i)]$$
$$+\frac{1}{2}\sum_{k,\,j;\,j\neq i} r_{ki}^\alpha (r_{ji}^\beta - r_{ki}^\beta) S_{kj}^i \exp[i(\mathbf{k}_p\mathbf{r}_j - \mathbf{k}_q\mathbf{r}_i)], \qquad (5)$$

where $S_{kj}^i = \partial^2 f^i/\partial c_k \partial c_j$. Note that the last term of Eq. (5) is nonzero only when all three sites i, j, and k are different, and so it is present only when the nonpairwise contributions $F_{m>2}^{ij\ldots k}$ in Eq. (1) are taken into account such as the TCA terms F_4^{ijkl} [13].

For the $L1_2$ and $L1_0$ phases in face-centred-cubic (FCC) alloys, Eq. (2) includes waves with three vectors $\mathbf{k}_s$: $\mathbf{k}_1 = (100)2\pi/a$, $\mathbf{k}_2 = (010)2\pi/a$, and $\mathbf{k}_3 = (001)2\pi/a$, where a is the lattice constant [8–15]. The local order within APBs in these phases can be described by the distribution of amplitudes (η_1, η_2, η_3) of these waves of the type (ζ, η, η) and corresponds to tetragonal symmetry [6, 9, 11]. To illustrate the form of terms $g_{pq}^{\alpha\beta}$ in Eq. (5), we present their MFA and PCA expressions for this type of local order. The tensors $g_{pq}^{\alpha\beta}$ can be described in terms of their "transverse" and "anisotropic" components $g_{pq}^\perp = g_{pq}^{22} = g_{pq}^{33}$ and $g_{pq}^a = (g_{pq}^{11} - g_{pq}^{22})$. Using, for simplicity, the 2-neighbor-interaction model $v_{n>2} = 0$ one obtains in the MFA

$$g_{\zeta\zeta}^\perp = -\frac{1}{2}a^2 v_2; \quad g_{\zeta\zeta,\,\eta\eta}^a = \pm\frac{1}{2}a^2 v_1;$$
$$g_{\eta\eta}^\perp = \frac{1}{2}a^2(v_1 - 2v_2); \qquad (6)$$
$$g_{cc}^\perp = -\frac{1}{2}a^2(v_1 + v_2); \quad g_{cc}^a = g_{\eta c,\,\zeta c,\,\eta\zeta}^{\perp,\,a} = 0,$$

while the PCA expressions for $g_{pq}^\perp$ and g_{pq}^a are:

$$g_{\zeta\zeta,\,cc}^\perp = \frac{1}{4}a^2(-\varphi_1^+ \pm \psi_1^+ - \chi_2^+ - \varphi_2^{dd}); \quad g_{\zeta c}^a = \frac{1}{4}a^2\varphi_1^-;$$
$$g_{\zeta\zeta,\,cc}^a = \frac{1}{4}a^2(\varphi_1^+ \pm \psi_1^+); \quad g_{\zeta c}^\perp = \frac{1}{4}a^2(-\varphi_1^- - \chi_2^+ + \varphi_2^{dd}); \qquad (7)$$
$$g_{\eta\eta}^\perp = \frac{1}{2}a^2(\varphi_1^{ab} - 2\chi_2^+); \quad g_{\eta\eta}^a = -\frac{1}{2}a^2\varphi_1^{ab};$$
$$g_{\eta\zeta,\,\eta c}^\perp = \frac{1}{4}a^2(\pm\psi_1^- - 2\varphi_2^-); \quad g_{\eta\zeta,\,\eta c}^a = \pm\frac{1}{4}a^2\psi_1^-.$$

Here, the plus or minus ($\pm$) corresponds to the first or second pair of lower indices in the left-hand sides of Eqs. (6) and (7);

$$\varphi_n^{ij} = -Tf_n/R_n^{ij}; \quad \varphi_n^\pm = \frac{1}{2}(\varphi_n^{ab} \pm \varphi_n^{dd});$$
$$\psi_n^\pm = \frac{1}{2}(\varphi_n^{ad} \pm \varphi_n^{bd}); \quad \chi_n^\pm = \frac{1}{2}(\varphi_n^{aa} \pm \varphi_n^{bb}); \qquad (8)$$
$$R_n^{ij} = [1 + 2f_n(c_i + c_j - 2c_ic_j) + f_n^2(c_i - c_j)^2]^{1/2};$$

$f_n = \exp(-v_n/T) - 1$ is the Mayer function; and index i or j equal to a, b or d corresponds to the mean occupation c_i or c_j of one of three different sublattices:

$$c_a = c + \zeta + 2\eta; \quad c_b = c + \zeta - 2\eta;$$
$$c_d = c - \zeta. \qquad (9)$$

If the TCA is used, the nearest-neighbor contributions φ_1^{ij} in Eqs. (7) are replaced by the relevant tetrahedron contributions S_{ij}^i presented in [14]. For the B2 order, there is only one order parameter $\eta_s = \eta$ [9]; the terms $g_{pq}^{\alpha\beta}$ have cubic symmetry: $g_{pq}^{\alpha\beta} = \delta_{\alpha\beta}g_{pq}$, and the MFA and PCA expressions for g_{pq} are similar to those for $g_{pq}^\perp$ in Eqs. (6) and (7).

In the phase-field method, the terms $g_{pq}^{\alpha\beta}$ are assumed to be independent of local parameters η_r and so assumed to be zero at $p \neq q$ on "considerations of symmetry" [6–8]. Equations (6) and (7) show that it may correspond only to the simplest MFA, while, in

more accurate approaches, such as PCA and TCA, the dependences $g_{pq}^{\alpha\beta}(\eta_r)$ can be significant.

Let us now consider the case of a plane APB (or IPB), when parameters η_p in Eq. (2) depend only on the distance $\xi = \mathbf{rn}_0$, where $\mathbf{n}_0 = (\cos\alpha, \sin\alpha\cos\varphi, \sin\alpha\sin\varphi)$ is normal to the APB plane. To find the equilibrium structure, one should minimize functional (4) with respect to functions $\eta_p(\xi)$ at a fixed total number of atoms [2]. Let us first consider the APB between two B2-ordered domains. Then, the variational equations for the order parameter $\eta(\xi)$ and the concentration $c(\xi)$ have the form

$$\begin{aligned} &g_{\eta\eta}\eta'' + g_{\eta c}c'' + \frac{1}{2}g_\eta^{\eta\eta}(\eta')^2 + g_c^{\eta\eta}\eta'c' \\ &\quad + \left(g_c^{\eta c} - \frac{1}{2}g_\eta^{cc}\right)(c')^2 = \frac{1}{2}f_\eta; \\ &g_{\eta c}\eta'' + g_{cc}c'' + \left(g_\eta^{\eta c} - \frac{1}{2}g_c^{\eta\eta}\right)(\eta')^2 + g_\eta^{cc}\eta'c' \\ &\quad + \frac{1}{2}g_c^{cc} = \frac{1}{2}(f_c - \mu). \end{aligned} \tag{10}$$

Here, the prime means taking derivative with respect to ξ; the lower index η or c means taking derivative with respect to η or c; and μ is the chemical potential. At $\xi \longrightarrow \infty$, functions c and η tend to their equilibrium values c_0 and η_0 (c_0).

Multiplying the first and second equations (10), respectively, by η' and c' summing them, and integrating the result, one obtains the first integral of this system of equations

$$g_{\eta\eta}(\eta')^2 + 2g_{\eta c}\eta'c' + g_{cc}(c')^2 = \Omega(\eta, c), \tag{11}$$

where Ω is the nongradient part of the local excess grand canonical potential per atom,

$$\Omega = f(\eta, c) - f_0 - \mu(c - c_0), \tag{12}$$

and index zero at the function means its value at $\eta = \eta_0$ and $c = c_0$.

In what follows, it is convenient to consider the order parameter η as an independent variable, while c and Ω as its functions determined by Eqs. (10)–(12). Then the dependence $\eta'(\eta)$ is determined by Eq. (11),

$$\eta' = d\eta/d\xi = (\Omega/G)^{1/2}, \tag{13}$$

where G is $(g_{\eta\eta} + 2g_{\eta c}\dot{c} + g_{cc}\dot{c}^2)$ and $\dot{c}$ is $dc/d\eta$. Using Eq. (13), one can exclude η' from the system of Eqs. (10) and obtain the differential equation for $c(\eta)$, to be called the composition-order equation (COE):

$$\begin{aligned} &[\ddot{c}(g_{\eta c}^2 - g_{cc}g_{\eta\eta}) + \Phi]2\Omega/G \\ &= (\mu - f_c)(g_{\eta\eta} + g_{\eta c}\dot{c}) + f_\eta(g_{\eta c} + g_{cc}\dot{c}), \end{aligned} \tag{14}$$

where Φ is a linear function of derivatives g_r^{pq},

$$\begin{aligned} \Phi &= (g_{\eta c} + g_{cc}\dot{c})\left[\frac{1}{2}g_\eta^{\eta\eta} + g_c^{\eta\eta}\dot{c} + \left(g_c^{\eta c} - \frac{1}{2}g_\eta^{cc}\right)\dot{c}^2\right] \\ &\quad - (g_{\eta\eta} + g_{\eta c}\dot{c})\left(g_\eta^{\eta c} - \frac{1}{2}g_c^{\eta\eta} + g_\eta^{cc}\dot{c} + \frac{1}{2}g_c^{cc}\dot{c}^2\right). \end{aligned} \tag{15}$$

Because of the equilibrium conditions $f_\eta^0 = 0$, $f_c^0 = \mu$, function $\Omega(\eta)$ (12) at $\eta \longrightarrow \eta_0$ is proportional to $(\eta - \eta_0)^2$. Therefore, the initial value $\dot{c}(\eta_0)$ can be found by taking the $\eta \longrightarrow \eta_0$ limit of Eq. (14).

For the given solution $c(\eta)$ of COE, the coordinate dependence $\eta(\xi)$ is determined by integrating Eq. (13),

$$\xi = \xi_1 + \int_{\eta_1}^{\eta} d\eta(G/\Omega)^{1/2}, \tag{16}$$

where the reference point ξ_1 is determined by the choice of value $\eta_1 = \eta(\xi_1)$. For the symmetrical APB for which $\eta \longrightarrow \pm\eta_0$ at $\xi \longrightarrow \pm\infty$, functions c, Ω and G are even in η, and it is natural to set $\xi_1 = 0$ at $\eta_1 = 0$. But for an IPB separating the ordered and the disordered phases, values $\eta_1 \longrightarrow 0$ correspond to $\xi \longrightarrow (-\infty)$, and so ξ_1 should be chosen as some intermediate value η_1.

The surface energy σ and the surface segregation Γ is the excess of the grand canonical potential and of B atoms, respectively, per unit area [2]. Taking into account Eqs. (11)–(13), one obtains for the surface energy

$$\sigma = \frac{2}{v_a}\int_{\eta_{\min}}^{\eta_0} d\eta(G\Omega)^{1/2}, \tag{17}$$

where $\eta_{\min}$ is $(-\eta_0)$ for an APB and zero for an IPB, while the surface segregation is given by the expression

$$\Gamma = \frac{1}{v_a}\int_{-\eta_0}^{\eta_0} d\eta(c_0 - c)(G/\Omega)^{1/2}. \tag{18}$$

For a symmetrical APB, the integral in Eq. (17) or (18) can be written as twice the integral over positive η.

Relations similar to Eqs. (11)–(18) can also be derived for phases with several order parameters, such as the $L1_2$ or $L1_0$ phase. In particular, for an APB separating two $L1_2$-ordered domains, the order parameters (η_1, η_2, η_3) have the form (ζ, η, η) mentioned above with the limiting values (η_0, η_0, η_0) and $(\eta_0, -\eta_0, -\eta_0)$ at $\xi \longrightarrow \pm\infty$. The variational equations and their first integral have the form analogous to Eqs. (10) and (11) but include three functions $c(\xi)$, $\zeta(\xi)$, and $\eta(\xi)$. It is again convenient to consider c and ζ as functions of η (for APBs in the $L1_0$ phase, c and η as functions of ζ) and obtain a system of equations for $c(\eta)$ and $\zeta(\eta)$ analogous to COE (14). Equations for $\xi(\eta)$ and c preserve

their form (16)–(18), but $G(\eta)$ now includes the derivative $\dot{\zeta} = d\zeta/d\eta$ and six functions g_{pq}, which are related to $g_{pq}^{\perp, a}$ in Eqs. (6) and (7) as follows:

$$g_{pq}(\alpha) = g_{pq}^{\perp} + g_{pq}^{a}\cos^2\alpha, \quad (19)$$

where α is the angle between the APB orientation and the local tetragonality axis. When the nearest-neighbor interaction v_1 much exceeds the remaining interactions (as in CuAu-based alloys [9–11]), the functions $g_{pq}(\alpha)$ are highly anisotropic, which is illustrated by Eqs. (6): $g_{\eta\eta} \sim \sin^2\alpha$; $g_{\zeta\zeta} \sim \cos^2\alpha$. It results in a notable anisotropy of distributions of APBs including the presence of many low-energy "conservative" APBs with $\alpha \simeq 0$ in the $L1_2$ phase and $\alpha \simeq \pi/2$ in the $L1_0$ phase, as well as a specific alignment of APBs in "twinned" $L1_0$ structures [9–11]. In more detail, COE and Eqs. (16)–(19) for the $L1_2$ and $L1_0$ phases will be discussed elsewhere.

Let us now discuss some applications of Eqs. (14)–(19). First, I consider the case where the equilibrium order parameter η_0 is small. Then, the function f in Eq. (4) can be written as the Landau expansion

$$f(\eta, c) = \varphi + a\eta^2 + b\eta^4 + d\eta^6, \quad (20)$$

where φ, a, b, and d are some functions of concentration c and temperature T. The equilibrium value η_0 is determined by the equation $f_\eta^0 = 0$, while the ordering spinodal $T = T_s(c)$ (the disordered phase-stability limit) is determined by the equation $a(c, T) = 0$. Small values η_0 under consideration correspond to the c_0, T points near the ordering spinodal, where $a(c_0, T)$ is small.

It is clear from both physical considerations and the results obtained below that the difference $(c - c_0)$ at small η_0 is also small. Therefore, functions $(f_c - \mu)$ and f_η in Eq. (14) can be expanded in powers of $(c - c_0)$, η and η_0:

$$f_c - \mu = a_c^0(\eta^2 - \eta_0^2) + \varphi_{cc}^0(c - c_0) + \ldots, \quad (21)$$

$$f_\eta = 4\eta b_0(\eta^2 - \eta_0^2) + 2\eta a_c^0(c - c_0) + \ldots \quad (22)$$

Here, φ_{cc}^0 is $(\partial^2\varphi/\partial c^2)_0$, and the dots mean terms of higher order in η_0^2. The analogous expansion of $\Omega(c, \eta)$ starts with terms bilinear in $(c - c_0)$ and $(\eta^2 - \eta_0^2)$, while for functions $g_{\eta c}$ and $\dot{c}$ the expansions start with terms linear in η. Thus, the terms with Ω and f_η in Eq. (14) are proportional to η_0^4, which are small compared to $(f_c - \mu) \sim \eta_0^2$, and COE is reduced to the equation $f_c = \mu$, which yields

$$c_0 - c(\eta) = (\eta_0^2 - \eta^2)(-a_c^0)/\varphi_{cc}^0. \quad (23)$$

Taking the derivative of equation $a(c, T) = 0$, one obtains $(-a_c^0) = T_s'\alpha$, where α is $(\partial a/\partial T)_0$ and $T_s' = dT_s/dc$. Thus, the surface segregation at APB is proportional to the ordering spinodal slope $T_s'(c_0)$, and so it decreases as it approaches the critical point where $T_s' = 0$.

Let us now assume that the alloy state c_0, T in the c, T plane is close to the second-order transition line $T_s(c)$ far from the possible tricritical points. Then, the higher-order terms in expansions (20)–(22) can be neglected, and for the function $\Omega(\eta)$ (12) this expansion yields

$$\Omega(\eta) = \tilde{b}(\eta_0^2 - \eta^2)^2; \quad \tilde{b} = b_0 - (\alpha T_s')^2/2\varphi_{cc}^0. \quad (24)$$

Using Eqs. (16)–(18) and (24), one obtains in this case for $\eta(\xi)$, $c(\xi)$, the APB energy σ and the segregation Γ:

$$\eta(\xi) = \eta_0\tanh(\xi/\delta), \quad c_0 - c(\xi) = \eta_0^2\lambda\cosh^{-2}(\xi/\delta),$$
$$\sigma = \frac{8}{3v_a}\eta_0^3(g\tilde{b})^{1/2}, \quad \Gamma = \frac{2}{v_a}\eta_0\lambda(g/\tilde{b})^{1/2}, \quad (25)$$

where λ is $\alpha T_s'/\varphi_{cc}^0$; g is $g_{\eta\eta}^0$; and $\delta = (g/\eta_0^2\tilde{b})^{1/2}$ is the APB width. These expressions generalize the earlier MFA results [12] to the case of any GL functional. The dependences $\eta(\xi)$ and $c(\xi)$ in Eqs. (25) are similar to those observed in the Monte Carlo study of segregation at APBs [5]. The temperature dependence of this segregation at small η_0 is sharper than for the APB energy: $\Gamma \propto \eta_0 \sim (T_s - T)^{1/2}$, while $\sigma \propto \eta_0^3 \sim (T_s - T)^{3/2}$. Equations (24) and (25) also show that the presence of segregation results in a renormalization of the Landau parameter b_0 entering the characteristics of APB to the lesser value $\tilde{b}$ given by Eq. (24). It results in a decrease in the APB energy σ and an increase in its width δ and segregation Γ under decreasing temperature T along the ordering spinodal $T = T_s(c)$.

The point c_0, T, at which both $a(c_0, T)$ in Eq. (20) and $\tilde{b}$ in Eq. (24) vanish, corresponds to the tricritical point c_t, T_t. At $T < T_t$, the second-order transition line $T_s(c)$ in the c, T plane splits into two binodals, $c_{bo}(T)$ and $c_{bd}(T)$, which delimit the single-phase ordered and disordered field, respectively. Such a tricritical point is observed, for example, in Fe–Al alloys [4]. At this point, the lowest order terms in Eqs. (22) and (24) vanish, so that one should consider the next-order terms, and function Ω (12) at small $x = (c - c_t)$ and $t = (T - T_t)$ takes the form

$$\Omega(\eta) = A(\eta_0^2 - \eta^2)^2(\eta^2 + h). \quad (26)$$

Here, $h = h(x, t)$ is a linear function of x and t, which can be written in terms of the binodal temperature derivative $c_{bo}' = dc_{bo}/dT$ as $h = \nu(x - tc_{bo}')$, while A and

ν are some positive constants. Using Eqs. (16)–(18) and (26), one obtains for the characteristics of APB near T_t

$$\eta(\xi) = \frac{\eta_0 \sinh y}{(\cosh^2 y + \alpha)^{1/2}}; \quad c_0 - c(\xi) = \frac{\lambda\eta_0^2(1+\alpha)}{(\cosh^2 y + \alpha)};$$
$$\sigma = \frac{J(\alpha)}{v_a}(gA\eta_0^4)^{1/2}; \quad \Gamma = \frac{2\lambda L(\alpha)}{v_a}(g/A)^{1/2}. \quad (27)$$

Here, y is $\xi/\tilde{\delta}$, α is η_0^2/h, and $\tilde{\delta}$, $L(\alpha)$ and $J(\alpha)$ are

$$\tilde{\delta} = [g/A\eta_0^2(h+\eta_0^2)]^{1/2};$$
$$L(\alpha) = \ln[(1+\alpha)^{1/2} + \alpha^{1/2}]; \quad (28)$$
$$J(\alpha) = \frac{1}{2\alpha^2}[(1+4\alpha)L(\alpha) + (2\alpha - 1)(\alpha + \alpha^2)^{1/2}].$$

The function $h(x, t)$ in Eqs. (26)–(28) is proportional to the distance in the c, T plane from point c_0, T to the binodal $c_{bo}(T)$, while η_0^2 is proportional to the distance to the ordering spinodal $T_s(c)$. Thus, at small $\alpha \ll 1$, Eqs. (26)–(28) turn into Eqs. (24) and (25) with $\tilde{b} = Ah$ and describe the critical behavior of APB near $T_s(c)$ discussed above. The opposite case, $\alpha \gg 1$, corresponds to the region of "wetting" APBs, which has recently received much attention [3, 6, 15]. The value $h = 0$ corresponds to the ordered state with $c_0 = c_{b0}(T)$, and then COE (14) describes an IPB between this state and the disordered state with $\eta_d = 0$ and $c_d = c_{bd}(T)$. Substituting Eq. (26) with $h = 0$ into Eqs. (16) and (17), one obtains for this IPB

$$\eta(\xi) = \frac{\eta_0}{(1+e^{-z})^{1/2}}; \quad c(\xi) - c_d = \frac{\lambda\eta_0^2}{(1+e^{-z})}; \quad (29)$$

$$\sigma_{APB} = 2\sigma_{IPB}. \quad (30)$$

Here, z is ξ/δ_1; $\delta_1 = (g/A)^{1/2}/2\eta_0^2$ is the IPB width; $\sigma_{IPB} = (gA\eta_0^2)^{1/2}/2v_a$ is the IPB energy; c_d is $c_0 - \lambda\eta_0^2$; and the coordinate $\xi_1 = 0$ in Eq. (16) is chosen at $\eta_1 = \eta_0/\sqrt{2}$, where $c(\eta_1)$ is $(c_0 + c_d)/2$. Equations (29) show that the order parameter η in the disordered phase decreases with increasing distance from IPB much more slowly than the concentration deviation: $\eta \sim (c - c_d)^{1/2}$. Equations (27)–(30) also show that, in the "wetting" regime of large α, the profiles $\eta(\xi)$ and $c(\xi)$ in Eq. (27) correspond to the presence, at $\xi_\pm = \pm\delta_1 \ln\alpha$, of two almost independent IPBs described by Eqs. (29). The total width $l \simeq (\xi_+ - \xi_-)$ and the segregation Γ for such APB are proportional to $\ln(1/h)$, while the energy difference $(\sigma_{APB} - 2\sigma_{IPB})$ is proportional to $h\ln(1/h)$, which are the usual dependences for the wetting regime [16]. Equations (27)–(30) specify these relations for the vicinity of tricritical points and enable one to follow the transition from the wetting to critical behavior of APBs under the variation of T or c_0.

Let us now apply Eqs. (14)–(l7) to derive wetting relation (30) for the phases with several order parameters, in particular, for the $L1_2$ phase in equilibrium with the $L1_0$ or the disordered FCC (A1) phase. This problem was discussed by a number of authors [3, 6, 15], but the general proof still seems to be absent. Let us first note that in consideration of IPB, the initial condition for COE (14) can be put in either the ordered or the disordered phase, i.e., for (c, η) values equal to either (c_0, η_0) or (c_d, 0), while the solution $c_{IPB}(\eta)$ for either of the choices is the same and unique. Therefore, in consideration of APB with the same initial values c_0, η_0, the solution $c_{APB}(\eta)$ coincides with $c_{IPB}(\eta)$ at $\eta > 0$; it is $c_{APB}(-\eta)$ at $\eta < 0$, and so Eq. (30) follows from Eq. (17). For the APB or IPB in the $L1_2$ phase, the local order can be described by the parameters (c, ζ, η) mentioned above, and their initial values in COE are (c_0, η_0, η_0), while the final values are (c_0, η_0, $-\eta_0$), (c_d, 0, 0), and (c_l, η_l, 0) for the case of an APB ($L1_2$ – A1) and IPB($L1_2$ – $L1_0$), respectively, where c_l and η_l correspond to the second binodal $L1_2 - L1_0$. Therefore, wetting relation (30) for the $L1_2$ – A1 or $L1_2$ – $L1_0$ phase equilibrium follows from COE and Eq. (17), just as for the single order-parameter case. Note, however, that at the given orientation $\mathbf{n}_0$ there are three types of APB in the $L1_2$ phase with the local order (η_1, η_2, η_3) of the form (ζ, η, η), (η, ζ, η), or (η, η, ζ), and the structure and energy for each type is generally different. Therefore, there are at least three types of IPB ($L1_2$ – A1) corresponding to a half of the relevant APB in the wetting limit. In the course of the kinetic wetting (for example, under the A1 $\longrightarrow$ A1 + $L1_2$ transformations studied in [7, 9]), each APB first transforms into two of "its own" IPBs, but, later these IPBs can evolve into other types.

The effects of anisotropy under wetting APBs in Eqs. (16)–(18) are described by the factor $G^{1/2}$, while the main contribution to $\Omega(\eta)$ is determined by the thermodynamic relations. In particular, singular contributions to σ and Γ under wetting $L1_2$–APB by the A1 or $L1_0$ phase correspond to the region of small η, where Ω has the same form as in Eq. (26), while $G(\eta)$ is reduced to its first term $g_{\eta\eta}$, since the functions $g_{\eta\zeta}$, $g_{\eta c}$, $\dot{\zeta}$, and $\dot{c}$, being odd in η, vanish at small η. Thus, the main contributions to the APB width and energy take the form

$$l \sim g_{\eta\eta}^{1/2}\ln(1/h);$$
$$(\sigma_{APB} - 2\sigma_{IPB}) \sim g_{\eta\eta}^{1/2} h\ln(1/h),$$

where the angular dependence $g_{\eta\eta}$ is given by Eq. (19). Therefore, the wetting effects can reveal a significant anisotropy, particularly, in short-range interaction systems. This agrees with some previous results [3, 6, 15].

I am grateful to I.R. Pankratov for assistance. This work was supported by the Russian Foundation for Basic Research, project nos. 00-02-17692 and 00-15-96709.

REFERENCES

1. J. W. Cahn and J. E. Hilliard, J. Chem. Phys. **28**, 258 (1958).
2. R. Kikuchi and J. W. Cahn, J. Phys. Chem. Solids **23**, 137 (1962); **27**, 1305 (1966).
3. R. Kikuchi and J. W. Cahn, Acta Metall. **27**, 1337 (1979).
4. S. M. Allen and J. W. Cahn, Acta Metall. **24**, 425 (1976).
5. F. Schmid and K. Binder, Phys. Rev. B **46**, 13553 (1992).
6. R. J. Braun, J. W. Cahn, G. B. McFadden, and A. A. Wheeler, Philos. Trans. R. Soc. London, Ser. A **355**, 1787 (1997).
7. Y. Wang, D. Banerjee, C. C. Su, and A. G. Khachaturyan, Acta Mater. **46**, 2983 (1998).
8. L. Proville and A. Finel, Phys. Rev. B **64**, 054104 (2001).
9. K. D. Belashchenko, V. Yu. Dobretsov, I. R. Pankratov, *et al.*, J. Phys.: Condens. Matter **11**, 10593 (1999); **11**, 10567 (1999).
10. K. D. Belashchenko, I. R. Pankratov, G. D. Samolyuk, and V. G. Vaks, J. Phys.: Condens. Matter **14**, 565 (2002).
11. V. G. Vaks, Pis'ma Zh. Éksp. Teor. Fiz. **73**, 274 (2001) [JETP Lett. **73**, 237 (2001)].
12. V. Yu. Dobretsov, G. Martin, F. Soisson, and V. G. Vaks, Europhys. Lett. **31**, 417 (1995).
13. V. G. Vaks and G. D. Samolyuk, Zh. Éksp. Teor. Fiz. **115**, 158 (1999) [JETP **88**, 89 (1999)].
14. V. G. Vaks, N. E. Zein, and V. V. Kamyshenko, J. Phys. F **18**, 1641 (1988).
15. Y. Le Bouar, A. Loiseau, A. Finel, and F. Ducastelle, Phys. Rev. B **61**, 3317 (2000).
16. B. Widom, J. Chem. Phys. **68**, 3878 (1978).

JETP Letters, Vol. 76, No. 2, 2002, pp. 99–103. Translated from Pis'ma v Zhurnal Éksperimental'noĭ i Teoreticheskoĭ Fiziki, Vol. 76, No. 2, 2002, pp. 110–114.

Soft Mode and Magnetic Phase Transition in PrNi

P. A. Alekseev[1]*, E. S. Klement'ev[1,2], P. Allenspach[2], Yu. I. Chumlyakov[3], V. N. Lazukov[1], and I. P. Sadikov[1]

[1]*Russian Research Center Kurchatov Institute, pl. Kurchatova 1, Moscow, 123182 Russia*

** e-mail: paval@isssph.kiae.ru*

[2]*LNS, Paul Scherer Institute, CH-5232 Villigen PSI, Switzerland*

[3]*Kuznetsov Physicotechnical Institute, pl. Revolyutsii 1, Tomsk, 634050 Russia*

Received June 11, 2002

Abstract—The spectrum of magnetic excitations in a single crystal of intermetallic compound PrNi was studied by inelastic neutron scattering. Experiment showed the substantial softening of some collective magnetic excitation modes near the ferromagnetic ordering temperature $T_c \approx 20$ K. The result is analyzed within the framework of a model that describes the magnetic phase transition in systems with induced magnetic moment. *© 2002 MAIK "Nauka/Interperiodica".*

PACS numbers: 75.30.Kz; 61.12.Ex

As a rule, rare-earth compounds based on non-Kramers ions, i.e., ions with a nonmagnetic (typically singlet) ground state in the crystal electric field (CEF), remain paramagnetic down to very low temperatures. However, in some cases, ferromagnetic ordering at $T_c \sim$ 10–20 K is observed in the compounds where the ground state should be nonmagnetic (Pr_3Tl, $PrAl_2$, and PrNi).

To explain this phenomenon, the concept of induced magnetic moment is used [1]. According to this concept, the magnetic ordering in the systems with a singlet ground state can occur only if the interion exchange interaction exceeds a certain critical value, which is associated, in particular, with the splitting of the 4*f* multiplet in CEF. This approach is basically different from the commonly used description of the ordering process in the presence of permanent magnetic moments in the crystal lattice. The analysis of the idealized two-level (singlet–singlet or singlet–triplet) schemes within the framework of mean-field random-phase approximation (MF-RPA) has shown that the transition should be accompanied by the appearance of a soft mode whose frequency is minimal at a wavevector corresponding to the magnetic Bragg peak (in ferromagnets, this corresponds to the center of Brillouin zone) and turns to zero at $T = T_c$.

A search for such a pronounced effect was undertaken in the Pr_3Tl ($T_c = 11$ K) compound [2], although the situation with the CEF levels (singlet–triplet + closely lying states) in this system is not closest to the simple model. This complication is due to the high (cubic) local symmetry of the Pr site. Unfortunately, measurements were not performed for a single crystal, and the neutron experiments were made on a three-axis spectrometer in the first Brillouin zone of a polycrystalline Pr_3Tl sample [2]. Although the dispersion of CEF excitations was observed, it virtually did not depend on temperature, contrary to the MF-RPA predictions. Additional consideration [3] showed that the expected softening did not occur because of the influence of excited states (other CEF levels), which should also contribute to the "central" ($E = 0$) peak. The experiments with quasi-elastic neutron magnetic scattering in this system [4] confirmed the presence of the central peak at $T \sim T_c$. In addition, it was found that the correlation radius decreased with an increase in the parameter $(T/T_c - 1)$ much slower than in conventional magnets.

The softening of magnetic modes in singlet systems was observed at different times in pure Pr under pressure (at $P = 0$, the exchange interaction comprises 80% of its critical magnitude), in the induced $PrNi_2Si_2$ antiferromagnet with incommensurate magnetic structure [5], and in the compounds close to HTSC (e.g., Pr_2CuO_4 [6]). The calculations were mainly carried out in the MF-RPA approximation with a single-ion CEF Hamiltonian. Interestingly, the dispersion of magnetic (singlet–triplet) excitation was observed in the SmS insulator [7], where the spectrum is formed not by the CEF but due to the spin–orbit interaction on the Sm^{2+} ion.

It should be emphasized that the original model of induced magnetism (isolated singlet–singlet complex) has been implemented and studied in none of the experiments. The key feature of the model, namely, the interrelation between the phase transition and the softening of a "paramagnon" in the center of Brillouin zone as T_c is approached from above, was also neither proved nor ruled out. That is, the concept of induced magnetism as a driving force of magnetic phase transition in the sin-

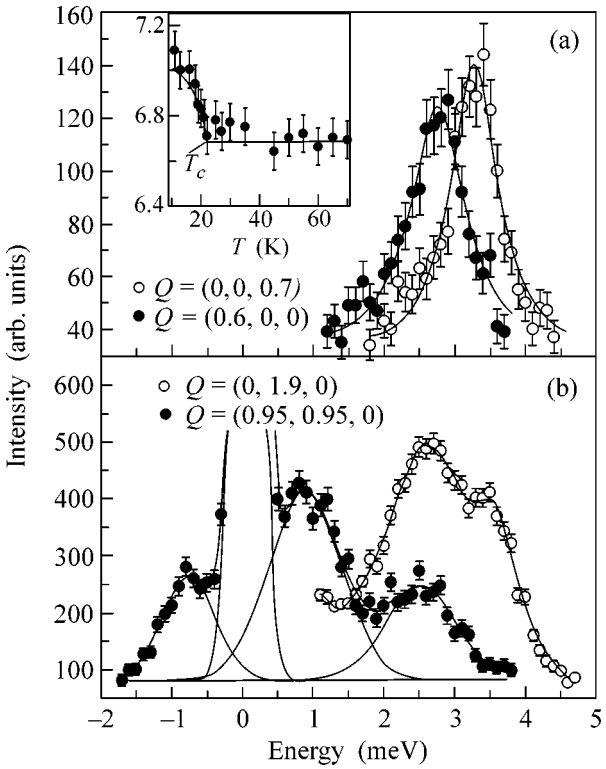

Fig. 1. Experimental neutron scattering spectra of a PrNi single crystal at T = 23 K, as measured for (a) **Q** ∥ [100], **q** ∥ [001] and (b) **Q** ∥ [110], **Q** ∥ [010]. The points (0, 0, 1) and (*h*, *h*, 0) are the centers of the Brillouin zone, and the points (2*h* + 1, 0, 0) and (0, 2*k* + 1, 0) correspond to the zone boundaries. Inset: temperature dependence of the intensity of Bragg peak (200) in the neutron diffraction pattern.

glet systems has not been directly verified for the appropriate model systems. Naturally, the transition has also not been studied in detail as a phenomenon associated with the competition of the single-ion and many-particle effects. For this reason, it is reasonable to seek an appropriate example among low-symmetry systems. In principle, Pr_2CuO_4 could be a good candidate, because, experimentally, only a single strong transition between the orthorhombic CEF levels was observed. However, the exchange interaction between the RE ions in this compound is weak.

Among the known metallic systems, PrNi is quite remarkable. The intermetallic PrNi compound has orthorhombic structure, so that the degeneracy of the lower J = 4 multiplet is completely removed [8] and a number of singlet states arise. Nevertheless, this compound undergoes ordering at T_c = 20 K [9].

In this work, the results of neutron experiments on a PrNi single crystal are reported. They suggest that there is a dispersive magnetic excitation with an energy on the order of 3 meV, and one of the branches of this excitation softens at the center of the Brillouin zone as $T \longrightarrow T_c$. These results allow PrNi to be considered as a model system for the detailed study of the magnetic ordering mechanism in the compounds with a singlet ground state.

The PrNi compound crystallizes into the CrB-type structure (orthorhombic; space group *Cmcm*) with one crystallographic type of parametric sites for Pr and Ni, which differ only by the parameters Y_{Ni} = 0.42 and Y_{Pr} = 0.14 [10]. The unit cell contains two Pr ions and two Ni ions. The local symmetry of the Pr site (orthorhombic C_{2v}) completely removes the degeneracy of the ground spin–orbital multiplet J = 4, and nine singlet states appear in the crystal field. The total splitting was estimated at 7–8 meV from the spectra of neutron inelastic magnetic scattering from Pr^{3+} in LaNi [8].

A single-crystal sample of PrNi with a volume of ~2 cm^3 was grown by the Bridgman method in an alundum crucible. According to the neutron diffraction data, the mosaicity was about 0.5°. The lattice parameters determined from the diffraction experiment (a = 3.824 Å, b = 10.497 Å, c = 4.358 Å) were in a good agreement with the tabular data (a = 3.817 Å, b = 10.501 Å, c = 4.347 Å). The ferromagnetic ordering temperature T_c = 21.5 K was determined from the temperature dependence of the intensity of diffraction peak (200) (see inset in Fig. 1).

The neutron inelastic scattering experiments were conducted on a three-axis DRÜCHAL or TASP (LNS PSI) spectrometer with a SINQ neutron source at a fixed final neutron energy of 5.57 or 8.05 meV. To suppress the contribution from the higher-order analyzer reflections, a pyrographite filter was used. Measurements were made in the temperature range 23–70 K along the basic crystallographic directions [100], [001], [010], and [110]. The range of measured energy transfer was 0–7 meV. Depending on the crystallographic direction, one or two magnetic scattering peaks were observed. For example, a single peak was observed for each of the [100] and [001] directions (Fig. 1a), and two peaks were observed for the [110] (Fig. 1b) and [010] directions. The peak energies depended noticeably on the reduced wavevector **q**. The dispersion curves for magnetic branches were obtained using the Gaussian approximation for the peaks at temperature T = 23 K slightly above the phase transition. In Fig. 2, they are presented for all the directions studied. By the character of energy q dependence, the excitations can be divided into "optical" and "acoustic" modes. In Fig. 2, the experimental dispersion curves are also given for the same excitations at a higher temperature T = 70 K. One can see that, as the temperature increases, all excitations converge to the two virtually dispersionless modes with energies near 2.3 and 3.3 meV. A sharp decrease in energy of acoustic modes upon approaching T_c from above ([100] and [110] directions) at the center of Brillouin zone can be regarded as a qualitative manifestation of the softening of the frequency of dipolar magnetic excitation. This is precisely what is predicted by the models describing the phenomenon of induced magnetic ordering. In the case considered, the PrNi lat-

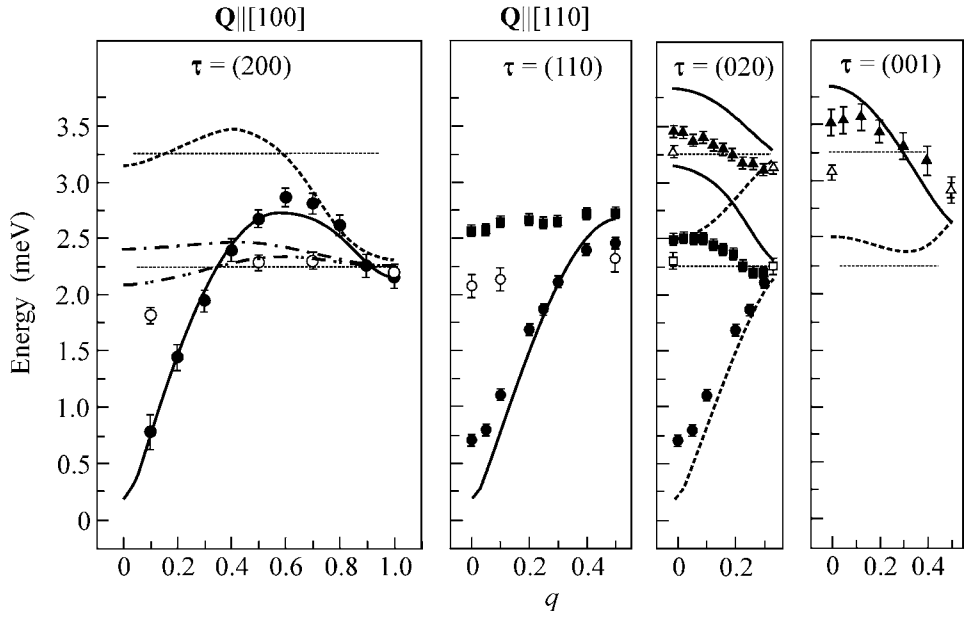

Fig. 2. Dispersion curves for energies of magnetic excitations in PrNi; symbols are for the experiment and lines are for the calculations. Only those branches are shown which are allowed for the polarizations M_1 and M_2 (see text). Dark symbols are for $T = 23$ K and empty symbols are for $T = 70$ K. Circles correspond to the acoustic excitations; triangles and squares correspond to the optical excitations. Solid lines are for the observable and dashed lines are for the unobservable transitions (in accordance with the structure factors calculated for a given site $\boldsymbol{\tau}$ of reciprocal lattice and for a given excitation branch); $T = 23$ K. For the [100] direction, the same excitations are shown by the dotted-and-dashed lines for $T = 70$ K.

tice contains two magnetically active ions (Pr^{3+}) per unit cell, so that each of the single-ion excitations splits additionally into the acoustic and optical branches. Another important feature of the spectra is that different excitation modes are observed for different orientations of the wavevector Q about the crystallographic directions. This fact is likely caused both by the nature of these excitations, i.e., by the symmetry of wave functions of the parent crystal-field levels and, hence, by the type of matrix element (M_x, M_y, M_z, or their combination), and by the dynamic structure factors for the different sites in the reciprocal space, which are determined by the real structure of the crystal lattice. The experiments on determining the possible states in the crystal field were performed on a sample in which the magnetic ions Pr^{3+} were strongly diluted with the nonmagnetic La ions to reduce the exchange Pr– Pr interaction. Indeed, in the experiments with a polycrystalline $Pr_{0.05}La_{0.95}Ni$ sample, narrow magnetic peaks were observed at $T = 5$ K at energies of 2.3 and 3.8 meV; i.e., the transitions from the ground state to the excited singlet states of the Pr^{3+} ion occur in PrNi. Considering a slight difference in the parameters of the LaNi and PrNi lattices, one can assume that the states responsible for the excitations at $E = 2.3$ and 3.3 meV in PrNi at a temperature of ~70 K have the same nature.

Qualitatively, the temperature dependence obtained for the dispersion of magnetic excitations (paramagnons) agrees with the assumption about the formation of excitation spectrum under the joint effect of crystal field and exchange interaction in the RE sublattice, as suggested by the two-level model of induced magnetism.

To elucidate the nature of the observed features in the $\mathbf{q}$ dependences of excitation energies and intensities, the MF-RPA calculations were carried out for a two-ion lattice. In so doing, the Pr–Pr interaction was taken into account up to the next- nearest neighbors (exchange constants J_{n1} and J_{n2}) in either of the (identical) sublattices and up to the next-nearest neighbors between the sublattices (J_{p1} and J_{p2}) (Fig. 3). For the energy $\hbar\omega(\mathbf{q})$ and intensity $I(\boldsymbol{\tau}, \mathbf{q})$ of magnetic modes, the following expression was used [11]:

$$\left.\frac{\hbar\omega(\mathbf{q})}{\hbar\omega_0}\right|_{A,\,O} = \left[1 - \frac{M}{\hbar\omega_0}(J_n(\mathbf{q}) \pm \nu J_p(\mathbf{q}))\right]^{1/2},$$

where $\hbar\omega_0$ is the energy of single-ion excitation in the crystal field; A and O stand for the acoustic and optical mode, respectively; M is the squared modulus of matrix element for the corresponding dipolar transition; $J_n(\mathbf{q})$ and $J_p(\mathbf{q})$ are the intra- and inter-sublattice exchange parameters calculated by the standard method,

$$J_j(\mathbf{q}) \equiv \sum_i J_{ij} \sum_k e^{-i\mathbf{q}\mathbf{R}_{ik}},$$

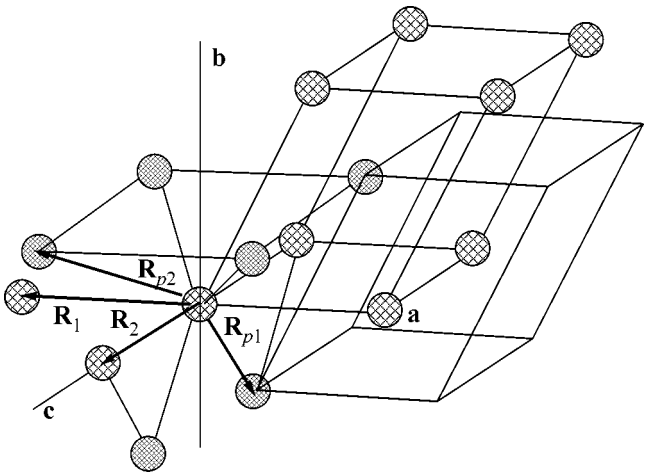

Fig. 3. Structure of the nearest surroundings in PrNi two RE sublattices (light and dark circles). R_{ij} are the distances between the ions inside and between the sublattices with exchange interaction constants J_{ij} (see text).

where $j = n$ and p (J_{ij} is the exchange constant for the ith coordination sphere formed by the atoms with radius-vectors $\mathbf{R}_{ik}$ and belonging to the jth sublattice); and ν stands for the sign of $J_p(\mathbf{q} = 0)$;

$$I_{A,O}(\boldsymbol{\tau}, \mathbf{q}) = c[1 \pm \cos(\varphi)],$$

$$\varphi(\boldsymbol{\tau}, \mathbf{q}) \equiv \boldsymbol{\tau} \cdot \mathbf{R}_p - \arctan\left\{\frac{\mathrm{Im}\,J_p(\mathbf{q})}{\mathrm{Re}\,J_p(\mathbf{q})}\right\};$$

where $\boldsymbol{\tau}$ is the reciprocal lattice vector for the chosen site in reciprocal lattice, $\boldsymbol{\tau} = \mathbf{Q} - \mathbf{q}$, and $\mathbf{R}_p$ is the basis vector of the RE sublattice (inter-sublattice radius-vector).

Four parameters J_{ji} (J_{n1}, J_{n2}, J_{p1}, and J_{p2}; see above) were determined by the χ^2 method from the dispersion curve for $\mathbf{Q} \parallel [100]$, which had the most complicated shape (with a maximum at $q \cong 0.6$). In so doing, the values of ω_{01} and ω_{02} were fixed, respectively, at 2.25 and 3.25 meV. The parameters M_1, M_2, and J_{ij} were unknown, because we did not determine the wave functions of the crystal-field levels. Because of this, M_1 and M_2 were varied about $\hbar\omega_{01}$ and $\hbar\omega_{02}$ within certain limits, and M_1 was found to be $M_1 = 0.85$ after the χ^2 minimization. From the ratio of peak intensities at $\hbar\omega_1 = 2.3$ meV and $\hbar\omega_2 = 3.8$ meV in the $Pr_{0.05}La_{0.95}Ni$ sample, the value of M_2 was found to be $M_2 = 0.5$. The matrix elements M_1 and M_2 were considered, respectively, mainly as $M_{z(c)}$ and $M_{x(a)}$, which corresponded to the behavior of mode intensities as functions of $\mathbf{Q}$ orientation in the reciprocal lattice. The fitting procedure for $\omega_A[q00]$ gave the following optimal values for J_{ij}: $J_{n1} = 0.58$ eV, $J_{n2} = -0.55$ meV, $J_{p1} = 0.6$ meV, and $J_{p2} = 0.35$ meV; i.e., the ferromagnetic Pr–Pr interaction in PrNi dominates. The dispersion weakens with increasing temperature. The dispersion curves of the acoustic and optical branches calculated for $\hbar\omega_{01}$ with $q \parallel [100]$ are shown in Fig. 2 for two temperatures ($T = 23$ and 70 K). For the geometry used in the experiment, $\mathbf{Q} \parallel \mathbf{q}$, $\boldsymbol{\tau} = (200)$, and the optical mode (dashed lines) had zero intensity, and so this was not detected. In the remaining panels in Fig. 2, the computational results are presented for the dispersion of acoustic and optical modes with the parameters J_{ij} given above determined by fitting ω_A in the [100] direction. Only those modes are shown for which the matrix elements M_1 and M_2 are nonzero in the corresponding directions.

The absence of experimentally observed excitations associated with ω_2 for $\mathbf{Q} \parallel [110]$ is likely caused by the strong anisotropy of reciprocal lattice; i.e., the [110] direction is close to [100], and, correspondingly, J_x does not show up in measurements, so that the $\omega_{2A,O}$ modes are not shown in the figure (as is well known, the neutron scattering intensity is determined by the $\mathbf{J}$ component perpendicular to $\mathbf{Q}$). The solid and dashed lines correspond to the modes with, respectively, nonzero and zero intensities, according to the calculated dynamic structure factor.

These results suggest that the experimental data are well reproduced by the model chosen: the character of mode dispersion and "observability" is consistent with the experimental data for all four calculated directions. The largest quantitative distinctions are obtained for the optical mode in the [110] direction.

On the whole, the actual symmetry of the RE ion surroundings in the crystal, together with the presence of two RE ions in the unit cell, can provide the observed features in the $\mathbf{q}$ dependence of excitation energies and intensities.

The main results of this work are as follows:

(i) a soft mode associated with the transition to the ferromagnetically ordered state was observed experimentally in a rare-earth intermetallic compound with a singlet ground state;

(ii) the properties of PrNi in the paramagnetic phase are well described by the MF-RPA model. This system is promising for a detailed study of the unusual mechanism of magnetic ordering in compounds based on the non-Kramers ions.

We are grateful to O.D. Chistyakov and N.B. Kol'chugina for assistance in sample preparation and to L.A. Maksimov for discussions. This work was supported by the state program NIKS and the Russian Foundation for Basic Research, project no. 00-15-96712.

REFERENCES

1. B. R. Cooper, *Magnetic Properties of Rare Earth Metals*, Ed. by R. J. Elliott (Plenum, London, 1972), p. 17.

2. R. J. Birgeneau, J. Als-Nielsen, and E. Bucher, Phys. Rev. B **6**, 2724 (1972).
3. T. M. Holden and W. J. L. Buyers, Phys. Rev. B **9**, 3797 (1974).
4. J. Als-Nielsen, J. K. Kjems, W. J. L. Buyers, *et al.*, J. Phys. C **10**, 2673 (1977).
5. J. A. Blanko, R. M. Niklow, and D. Schmitt, Phys. Rev. B **56**, 11666 (1977).
6. I. W. Samarlin, J. W. Lynn, T. Chattopadhyay, *et al.*, Phys. Rev. B **51**, 5824 (1995).
7. S. M. Shapiro, R. J. Birgeneau, and E. Bucher, Phys. Rev. Lett. **34**, 470 (1975).
8. P. A. Alekseev, E. S. Klement'ev, V. N. Lazukov, *et al.*, Pis'ma Zh. Éksp. Teor. Fiz. **63**, 947 (1996) [JETP Lett. **63**, 1000 (1996)].
9. G. Fillion, D. Gignoux, F. Givord, *et al.*, J. Magn. Magn. Mater. **44**, 173 (1984).
10. J. I. Finney and A. Rozenzweig, Acta Crystallogr. **14**, 69 (1961).
11. I. Jensen and A. R. Mackintosh, *Rare Earth Magnetism: Structures and Excitations* (Clarendon, Oxford, 1991).

Translated by V. Sakun